

Vibrational state to state collision induced intramolecular energy transfer $N_2(A\ 3\Sigma^+u, v'' \rightarrow B^3\Pi_g, v')$

R. Bachmann, X. Li, Ch. Ottinger, A. F. Vilesov, and V. Wulfmeyer

Citation: *J. Chem. Phys.* **98**, 8606 (1993); doi: 10.1063/1.464469

View online: <http://dx.doi.org/10.1063/1.464469>

View Table of Contents: <http://jcp.aip.org/resource/1/JCPSA6/v98/i11>

Published by the American Institute of Physics.

Additional information on J. Chem. Phys.

Journal Homepage: <http://jcp.aip.org/>

Journal Information: http://jcp.aip.org/about/about_the_journal

Top downloads: http://jcp.aip.org/features/most_downloaded

Information for Authors: <http://jcp.aip.org/authors>

ADVERTISEMENT

physicstoday

Comment on any
Physics Today article.

Measured energy in Japan
David von Seggern
(vonneg@seismo.unr.edu) University of Nevada
July 2012, page 10
DIGITAL OBJECT IDENTIFIER
<http://dx.doi.org/10.1063/PT.3.1619>
The article by Thorne Lay and Hiroo Kanamori is an interesting one. It discusses the energy release of the 1994 Northridge earthquake, which was estimated to be about 10¹⁵ J. This is a large amount of energy, but it is only a fraction of the energy released by the 1964 Chilean earthquake, which was estimated to be about 10¹⁷ J. The authors of the article use a relation for seismic energy release that depends on the strain energy release, which is a variable that depends on the fault plane. Accounting for total strain energy release would increase the earthquake energy number by orders of magnitude. Despite the catastrophic damage potential of nuclear bombs, the forces of nature occasionally unleash much larger energy releases. Although the nuclear bombs are under our control, earthquakes, volcanic eruptions, and extreme weather events are not. However, by judicious preparation and avoidance measures, humans can significantly diminish the damage of natural events.

Comment on this article
By the act of hitting a ball with a bat, one calculates the force energy to deliver the ball to its new location, but one must also take into account that the ball extended its energy release to that which became struck by the ball as its momentum ceased and passed energy to the struck item. Therefore the parameters of the damage extend into the future when the received energy to that pushed upon later becomes released in a new event. Perhaps calculations of one added that in while another's calculations did not. E.M.C.
Written by Edgar McCarroll, 14 July 2012 19:59

Vibrational-state-to-state collision-induced intramolecular energy transfer $\text{N}_2(A\ ^3\Sigma_u^+, v'' \rightarrow B\ ^3\Pi_g, v')$

R. Bachmann, X. Li,^{a)} Ch. Ottinger, A. F. Vilesov,^{b)} and V. Wulfmeyer^{c)}
Max-Planck-Institut für Strömungsforschung, Bunsenstrasse 10, 3400 Göttingen, Germany

(Received 8 October 1992; accepted 3 February 1993)

Absolute cross sections for collision-induced intramolecular energy transfer from the metastable $A\ ^3\Sigma_u^+$ state into the radiating $B\ ^3\Pi_g$ state of N_2 have been measured for the first time under single-collision conditions, using a thermal energy molecular beam of $\text{N}_2(A)$. The collision partners studied were the five rare gases, H_2 , N_2 , NO , and O_2 . The product vibrational levels ($B, v'=4-10$) were separated using spectrally resolved detection by means of filters as in our earlier related work [R. Bachmann, X. Li, Ch. Ottinger, and A. F. Vilesov, *J. Chem. Phys.* **96**, 5151 (1992)]. In addition, in the present study the contributing reactant state vibrational levels (A, v'') were labeled, using optical pumping by a specially developed broad-band (~ 1 nm) pulsed tunable dye laser. A depletion of up to 30% of a given v'' level could be achieved, about one-half of the theoretical maximum, at a pump pulse energy of 4 mJ. This quantity was also measured directly using a second synchronized probe laser. Pumping on a particular A, v'' level reduces the emission from the collisionally coupled B, v' level by an amount which is a measure of the state-to-state cross section. Quasiresonant energy transfer was found to be strongly preferred, the cross section decreasing exponentially with an increasing energy gap. Absolute cross sections were obtained from a simultaneous measurement of the intensity of the fluorescence induced by the laser pumping of the selected A, v'' level, with corrections for predissociation of the excited upper state. Cross sections on the order of $0.1\ \text{\AA}^2$ for He to $15\ \text{\AA}^2$ for Xe were found for closely resonant ($\Delta E \approx 100\ \text{cm}^{-1}$) processes. These results as well as our earlier, absolute measurements of the analogous intramolecular $\text{N}_2(W \rightarrow B)$ transfer, are discussed in terms of interaction potential models.

I. INTRODUCTION

Collision-induced intramolecular coupling within the triplet manifold of N_2 , especially the $B\ ^3\Pi_g$, $A\ ^3\Sigma_u^+$, and $W\ ^3\Delta_u$ states, has long been recognized as an important mechanism of energy conversion in any system involving excited nitrogen.¹⁻¹⁸ The vibrational levels of these states, in the following denoted as B, v' , A, v'' , and W, v , respectively, are shown in Fig. 1. It is seen that the collision-induced transitions studied in this work, from the long-lived $\text{N}_2 A$ and W states into the radiating B state, concern levels which store very large amounts of energy, up to almost 10 eV. The energy conversion processes are therefore clearly of great practical importance. Moreover, Fig. 1 illustrates the wide variety of elementary reactions which are involved, ranging from endothermic to exothermic energy transfer collisions, for two different electronic reactant states. The N_2 triplet system therefore provides a testing ground for the traditional phenomenological descriptions such as the exponential gap model, and at the same time it poses a challenge to develop further and extend the as yet sparse accurate theoretical treatment of intramolecular non-adiabatic collision-induced transitions in small molecules.

Previous studies employing laser excitation of the $\text{N}_2(B, v')$ levels in static or flow systems¹⁰⁻¹⁷ have demonstrated that the $\text{N}_2(B, v')$ state is collisionally coupled to other members of the triplet manifold. However, since only the $\text{N}_2(B, v')$ state was monitored in these experiments, the partner states coupling with a particular B, v' level and their relative importance could not be well specified. In Refs. 10-12, 15, and 16 the W state was proposed to be the most important coupling partner of the B state, while the role of the A state remained less clear. A very recent paper on the quenching of $\text{N}_2(B)$ ⁹ contains many references to previous work. In none of these studies was a large variety of collision gases systematically explored.

An attempt to study state selectively the $A, 7-B, 0$ collisional coupling in a pulsed N_2 discharge was made in Ref. 18. It was found that the time-resolved decay of the afterglow emission from $B, v'=0$ is multiexponential, and one of four components was ascribed to $A-B$ collisional coupling. This was confirmed by laser depopulation of the $A, 7$ level, which diminished the intensity of this particular decay component. However, the complexity of the processes determining the population of the excited states in a discharge afterglow permitted only a rough estimate of the coupling rate constant.

In our previous work¹⁹ the collisional coupling of the nitrogen triplet manifold states was for the first time studied under single collision conditions, and for a large number of collision partners. A molecular beam containing excited species N_2^* was crossed by a secondary atomic or

^{a)}Present address: Dalian Institute of Chemical Physics, Dalian, P.O. Box 110, Peoples Republic of China.

^{b)}Fellow of the Alexander von Humboldt Foundation, on leave from Institute of Physics, St. Petersburg State University, St. Petersburg, 198904, Russia.

^{c)}Present address: MPI für Meteorologie, 2000 Hamburg 13.

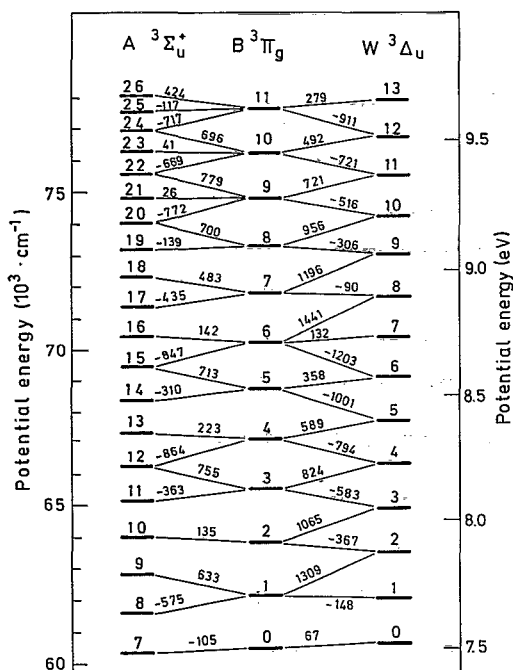


FIG. 1. Energy level diagram of three collisionally coupled triplet states of nitrogen (reproduced from Ref. 19 for convenience). The ordinate scales refer to the $N_2(X, v=0)$ ground state. The energy differences (in cm^{-1}) between vibrational levels of the B state and those of the A and W states are indicated.

molecular beam or passed through a target gas cell, resulting in relatively intense $N_2(B \rightarrow A)$ emission from the interaction region. The emission due to this collisional population of the B state levels is here referred to as "collision-induced afterglow" "CIAG," to distinguish it from the usual, spontaneous afterglow "AG" emitted from the N_2^* beam even in the absence of collisions. Measurements of the relative band intensities of the CIAG spectrum, in combination with a time of flight technique, allowed an analysis of the state specific energy transfer processes $N_2(A, v'') \rightarrow N_2(B, v')$ and $N_2(W, v) \rightarrow N_2(B, v')$. For both these reactions, relative cross sections were obtained as a function of v' and the collision partner. However, the assumption had to be made in each case that only a single reactant vibrational level contributes to the population of a given B, v' product level, namely, that one which is in closest resonance. The present work focuses on this point. Using a specially developed broad-band dye laser, the vibrational levels v'' of the $N_2(A)$ component of the beam were selectively depopulated, and the corresponding reduction of the subsequent CIAG $N_2(B \rightarrow A)$ emission was observed. In this way the previous postulate of nearly resonant $A \rightarrow B$ transfer could be quantitatively substantiated. This optical pumping technique was also tried on the $N_2(W)$ beam component, by scanning the laser through the expected range of the hitherto unobserved $N_2(G^3\Delta_g \leftarrow W^3\Delta_u)$ transition. However, neither could a reduction of the $B \rightarrow A$ CIAG signal be detected nor indeed any laser-induced fluorescence, probably on account of a small transition moment.

Absolute state-specific cross sections have also been

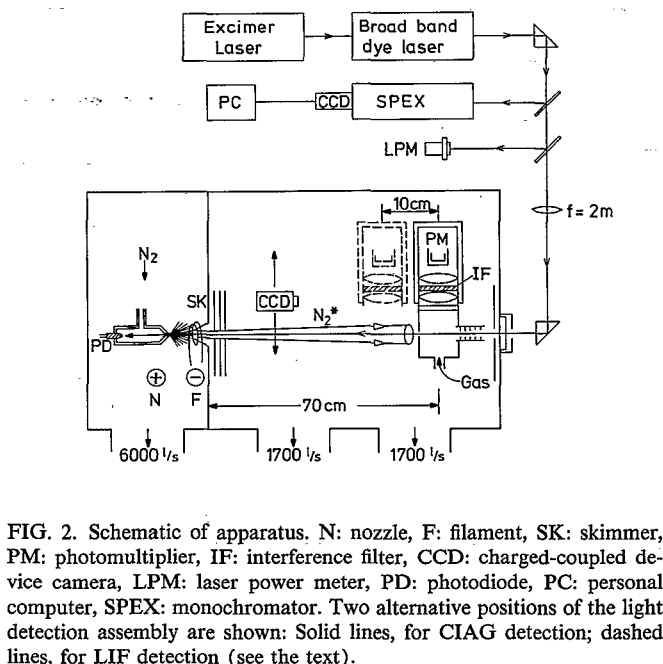


FIG. 2. Schematic of apparatus. N: nozzle, F: filament, SK: skimmer, PM: photomultiplier, IF: interference filter, CCD: charged-coupled device camera, LPM: laser power meter, PD: photodiode, PC: personal computer, SPEX: monochromator. Two alternative positions of the light detection assembly are shown: Solid lines, for CIAG detection; dashed lines, for LIF detection (see the text).

reported in Ref. 19, but only for the $N_2(W \rightarrow B)$ collisional coupling. In this case the reactant W, v levels could be directly monitored via the spontaneous beam afterglow. For the A, v'' levels there is no such convenient monitor signal from the beam. However, laser-induced fluorescence (LIF) can be used instead. In the present work this technique was employed to measure absolute state-specific cross sections also for the $N_2(A \rightarrow B)$ collisional coupling. They were derived by relating the dip of the CIAG intensity to the intensity of the LIF excited by the laser pulse which depopulated the selected A, v'' level.

II. EXPERIMENT

The experimental arrangement used in this work is similar to that described in Refs. 19–23, with the addition of the laser pumping. It is schematically shown in Fig. 2. Excited nitrogen molecules are generated by means of a dc discharge through the beam just outside the nozzle. Measurements of the N_2^* velocity distribution²³ gave a most probable velocity of $\bar{v}=960$ m/s, corresponding to a mean laboratory-frame N_2^* translational energy of 120 meV or 1060 cm^{-1} . The rotational temperature of the $N_2(A)$ molecules is about 140 K.²³ The mean relative energy of the $N_2^* + M$ collisions for some typical target gases is $E_{c.m.}(H_2)=360 \text{ cm}^{-1}$, $E_{c.m.}(Ar)=750 \text{ cm}^{-1}$, $E_{c.m.}(Xe)=925 \text{ cm}^{-1}$.

The collision-induced afterglow was produced by passing the molecular beam through a collision cell positioned on the beam axis. Its design details are described in Ref. 19, except the diameter of the entrance and exit diaphragms was now 3.5 mm. The collision cell was in this work placed at the largest possible distance ($s=70$ cm) from the discharge, thereby ensuring that the contribution from the long-lived A state^{24,25} dominates in the CIAG. The other contributing state, $N_2(W)$, decays largely by radiative transitions during the time of flight from the beam source

TABLE I. Observed $N_2(B-A)$ bands and parameters of the interference filters^a used to isolate them.

$B, v' \rightarrow A, v''$	$\lambda_{\max}, \text{nm}^b$	$\Delta\lambda, \text{nm}^c$	Transmission, %
18–17	653.4	3.3	34
17–13	551.5	7.2	47
10–7	631.7	3.0	44
9–6	638.5	3.0	40
8–5	646.0	2.8	35
7–4	653.4	3.3	34
6–4	725.0	3.9	43
5–3	735.9	3.8	36
4–2	750.0	10.0	55

^aDiameter 50 mm, except 25 mm for the second and third filter.^bWavelength at peak transmission.^cFull width at half-maximum.

to the collision cell.^{19,20,25,26} The number density of the target species in the cell was directly measured by means of an ion gauge (Leybold–Heraeus, IM 30), with gas-dependent correction factors.²⁷ The accuracy of this procedure was checked for several gases using a Baratron model 127 pressure gauge (specified absolute accuracy 0.25%), which gave an agreement within better than 10%. The base pressure in the main chamber was 10^{-6} mbar, rising to typically about $5 \cdot 10^{-6}$ mbar with the collision cell filled.

Narrow-band interference filters (Schott) were used to isolate the CIAG emission from a desired B, v' level. Spectral transmission functions of these filters were specially measured and their parameters are given in Table I, along with the selected emission bands. Contributions from close-lying, unwanted bands are $\leq 5\%$, as was shown by calculations including the estimated blueshift of the transmission for non-normal incidence. The luminescence was detected by a thermoelectrically cooled RCA C 31034-A02 photomultiplier in conjunction with a photon counter (SSR 1120). Time-resolved CIAG signals were measured using an ultrafast (≥ 5 ns/channel, 64k channels) multi-channel time of flight module (CMTE, model 7885). The typical count rate was, depending on the collision gas and especially on the B, v' level under study, about 0.01–0.5 per channel (of width 5.12 μs) per laser pulse.

Partial depopulation of selected A, v'' levels in the reactant beam was performed using a home-made broadband dye laser²⁸ pumped by a XeCl excimer laser (Questek model 2240, pulse energy about 80 mJ, repetition rate 50 Hz). In most experiments it was operated with Coumarin 307 dye. Typical output parameters were: bandwidth $\Delta\lambda \approx 0.5$ –1 nm, pulse energy in the observation region $E \approx 4$ mJ. The laser pulse energy was measured by a Scientech 365 power meter, and was continuously monitored during the experiments by a Gentech Model ED 100A energy detector. The laser beam propagated antioaxially to the N_2 molecular beam. It was slightly focused by an $f=200$ cm lens located outside the vacuum chamber (Fig. 2). The position and diameter of the laser beam were measured directly *in situ* by means of a CCD camera (Philips LDH 4460) which could be moved into the beam during operation. The high spatial resolution of the CCD detection was

especially useful in the experiments reported in the Appendix A, where two separate, narrow laser beams were arranged so as to overlap coaxially. In order to facilitate the adjustment of the laser beam and to monitor it continuously during the measurements, a photodiode was used, which was placed on the axis behind the nozzle in the gas inlet tube. A small portion of the laser beam was diverted via a beam splitter, and the spectrum of the laser emission was measured by the combination of a monochromator (SPEX 1702, 0.75 m) and a CCD camera (Sony XC 77 CE) interfaced to a PC. This arrangement allows simultaneous measurements of spectral intervals 40 nm wide with a resolution of 0.08 nm. During the measurements the laser spectrum was recorded digitally and also directly displayed on a TV screen. The spectral contour of individual laser pulses was stable from shot to shot to within less than 10% of its half-width. Mode structure was not detected, but even if present it would have been of no concern due to the large number of rotational lines (≈ 200) which were simultaneously excited. This was supported by the observation that the results were insensitive against slight detuning of the laser.

The broad-band laser was tuned to transitions in the $N_2(B-A)$ $\Delta v=5$ sequence near 510 nm in order to depopulate selectively one of the A, v'' levels in the range $v''=12$ –22. This corresponds to laser excitation of the $B, v'=17$ –27 levels, which lie above the N_2 dissociation limit. The lifetimes of these levels are largely determined by predissociation via the $N_2 A' {}^5\Sigma_g^+$ state, having rate constants γ_{prediss} in the range 1 – $20 \times 10^6 \text{ s}^{-1}$.^{23,29} They are thus comparable to or in most cases shorter than the extrapolated radiative lifetime of about 4 μs .³⁰ Therefore, any backpopulation of the A, v'' levels by the $B-A$ radiative transitions is usually negligible. A degree of depopulation as high as 30% can easily be achieved for most of the $N_2(A, v'')$ levels. Direct measurements of this quantity, by means of pump and probe lasers, are reported in Appendix A.

The usual experimental routine to measure relative cross sections for the intramolecular collision-induced $N_2(A, v'' \rightarrow B, v')$ energy transfer was the following. Admitting the collision gas at a pressure of about $3 \cdot 10^{-3}$ mbar to the collision cell, CIAG emission was observed from a particular $N_2(B, v')$ product level, as selected by the suitably chosen filter. Then the broad-band laser was tuned to a fixed wavelength centered on an $N_2(A-B)$ absorption band which originates from a A, v'' reactant level lying energetically near the selected B, v' level. The optical pumping by the laser resulted in a dip of the time-resolved CIAG emission signal. This dip is a relative measure of the desired cross section. The experiment was then repeated with the laser tuned to other nearby v'' levels (but still within the $\Delta v=5$ sequence), and the corresponding CIAG intensity dips, if any, were measured. They were each normalized to the respective absorption Einstein coefficients, as integrated over the laser bandwidth, and to the laser power. These same steps were then gone through for the other collision gases. Finally, changing the interference filter to the next v' to be studied, the entire procedure was repeated. In this way a large array of relative cross section

data as a function of v' and v'' as well as of the collision partner was collected.

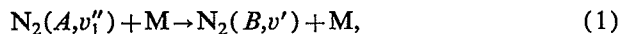
For measurements of absolute cross sections, the photomultiplier was positioned so as to view a portion of the laser-irradiated beam outside the collision cell, in order to detect the LIF signal from the pumped $N_2(A, v'')$ levels. The cross sections can then be found from the ratio of the CIAG intensity dip and the time-integrated LIF signal as described below.

Although the band width of the pump laser covered the absorption lines from most of the rotational/fine structure states of a given A, v'' level to be depleted, it did not necessarily depopulate all of these states by equal amounts. Also for different v'' levels the "centroid" of the pumping may have been somewhat different. However, this is unimportant for the study of the collisional energy transfer. In separate experiments using a narrow-band pump laser it could be shown for the particular case of the transfer $A, 10 \rightarrow B, 2$ that it is, in fact, independent of the rotational and fine structure state of the reactant molecule, within the experimental accuracy of $\pm 15\%$.³¹

III. RESULTS

A. Depopulation analysis

At $s=70$ cm, the CIAG observed in the collision cell is mainly due to reactions of the metastable A -state molecules



The $N_2(W)$ component of the beam has largely decayed at this distance from the source,¹⁹ and it contributes significantly only to the CIAG from the low v' levels, e.g., 7%, 32%, and 15% for $v'=6, 5$, and 4, respectively.¹⁹ The intensity of the emission in reactions (1) and (2) can be expressed as

$$I_{v'} = c \cdot [M] \cdot \bar{v}_{\text{rel}} \cdot \left(\sum_{v''} \sigma_{A, v''}(v') \cdot [A, v''] + Z_{v'} \right), \quad (3)$$

where c is a constant which includes geometry factors and the detection sensitivity, $[M]$ is the number density of the collision gas, and \bar{v}_{rel} is the relative velocity of the collision partners. $\sigma_{A, v''}(v')$ are cross sections for population of a B, v' level from the various A, v'' levels via reaction (1), and $[A, v'']$ are the corresponding number densities of the A, v'' species in the observation region. $Z_{v'}$ is a constant contribution to the CIAG intensity from other sources, e.g., the residual contribution of the W state or some background emission. The decrease of $I_{v'}$ due to laser depopulation of a given level A, v'' by an amount $\Delta[A, v'']$ is, from Eq. (3)

$$\Delta I_{v'} = c \cdot [M] \cdot \bar{v}_{\text{rel}} \cdot \sigma_{A, v''}(v') \cdot \Delta[A, v'']. \quad (4)$$

Thus this difference signal depends only on the particular A, v'' level being depleted by the laser. Note especially that any contribution to the CIAG from the W state also cancels out.

Figure 3 shows a typical example of the depopulation experiments. In this case $A, v''=16$ was depopulated in the

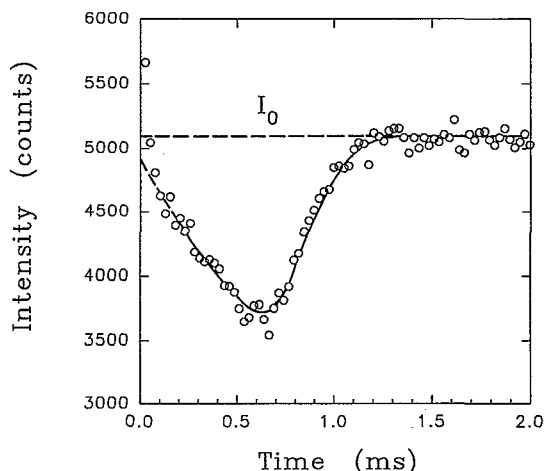


FIG. 3. Typical result of a time-resolved measurement of the CIAG (collision-induced afterglow) intensity. I_0 marks the steady-state CIAG intensity. A laser pulse at $t=0$ depletes the $A, v''=16$ level, which is collisionally coupled (collision gas Ar, cell pressure $3 \cdot 10^{-3}$ mbar) with the $B, v'=6$ level. The emission intensity from this level exhibits the transient dip shown, which is a measure of the state-to-state energy transfer cross section. Photon counts from 20 000 laser shots were accumulated, integration time per data point 25.6 μ s. Dashed line: Extrapolation of CIAG signal to $t=0$. Prior to the laser pulse, at $t < 0$, the signal level was constant at I_0 (not shown here for reasons of triggering). For details of the CIAG wave form see Appendix B.

transition $B, 21 \leftarrow A, 16$ at 508.5 nm and the CIAG was observed in the $B, 6 \rightarrow A, 4$ band at 725 nm. Since the levels $A, 16$ and $B, 6$ are in close resonance (Fig. 1), the $B, 6$ level is predominantly populated via the collision-induced energy transfer from $A, 16$. Therefore, laser depopulation of $A, 16$ diminishes the I_6 luminescence. The depopulation signal lasts for approximately 700 μ s which corresponds to the time of flight of the N_2^+ molecules from the discharge to the collision cell. More details on the form of the depopulation signal and magnitude of the depopulation can be found in Appendix B.

According to Fig. 3, a convenient measure of the CIAG intensity dip is the quantity

$$D_{v''}(v') = [I_0(v') - I_{\min}(v')]/I_0(v'), \quad (5)$$

where $I_0(v')$ and $I_{\min}(v')$ are, respectively, the base level and the minimum of the time-resolved CIAG emission from the (B, v') state. From Eq. (4), the observed magnitude of $D_{v''}(v')$ will be proportional to the depletion of the level A, v'' .

Our earlier molecular beam study¹⁹ of the collisional energy transfer $N_2(A \rightarrow B)$ according to Eqs. (1) and (2) was preliminary insofar as the individual reactant vibrational level could not be unequivocally distinguished by experimental means. Relative cross sections were obtained making the simplifying assumption that only closest-to-resonance levels contribute. The present work improves on this in two respects:

(a) The A, v'' levels participating in the population of a particular B, v' level are clearly labeled by laser pumping. If more than one level takes part, their relative contributions, given by the terms $\sigma_{A, v''}(v') \cdot [A, v'']$ in Eq. (3), are

measured separately. With the known vibrational distribution $[A, v'']$ from Ref. 23 this yields cross sections $\sigma_{A, v''}(v')$ in relative units.

(b) Absolute cross sections are then derived from additional LIF measurements.

Steps (a) and (b) are discussed in the following two sections.

B. Branching ratios

The relative contributions of the collisional population of a given B, v' level from the energetically favorable A, v'' levels can be described in terms of cross section "branching ratios." These were measured systematically in the following way.

After selecting the v' level by means of a suitable filter (see Table I), the laser was tuned so as to pump a particular v'' level, and the resulting CIAG dip $D_{v''}(v')$ was recorded (see, e.g., Fig. 3 for $v'=6$ and $v''=16$, a near-resonant pair).

From Eqs. (3), (4), and (5) it is seen that

$$D_{v''}(v') = \frac{G \cdot \sigma_{A, v''}(v') \cdot \Delta[A, v'']}{\sum_{v''} \sigma_{A, v''}(v') \cdot [A, v''] + Z_{v'}}, \quad (6)$$

i.e., $D_{v''}(v')$ is proportional to the product $\sigma_{A, v''}(v') \cdot \Delta[A, v'']$ of the desired cross section and the level depopulation. G is a constant factor allowing for the experimental geometry (see Appendix B). Repeating the experiment with the laser tuned to a different level v'' , the denominator of Eq. (6) remains unaffected. For each pumped level v'' , $\Delta[A, v'']$ is related to the population $[A, v'']$ itself by

$$\Delta[A, v''] = R_{v''} \cdot [A, v''], \quad (7)$$

where the depletion fraction $R_{v''}$ is numerically known from the respective theoretical absorption contours $B_{v''}(\lambda)$ (with London-Hönl factors from Ref. 32) and the laser spectrum $\rho(\lambda)$ as measured in each case (see Appendix C). For example, tuning the laser to deplete $v''=17, 18, 19$, the respective relative depopulations $R_{v''}$, in a particular run of experiments, were found from Eq. (C1) to be $R_{v''}=28.6\%$, 27.5% , and 27.8% . (The absorption Einstein coefficients $B_{v''}$ vary here only slightly with v'' within the $\Delta v=5$ sequence.) For $v''=20, 21$, and 22 the corresponding results were $R_{v''}=26.3\%$, 22.1% , and 17.1% .

Substituting Eq. (7) into Eq. (6), $D_{v''}(v')$ is then given in terms of $\sigma_{A, v''}(v') \cdot [A, v'']$. $[A, v'']$ is known in relative units.^{23,33} Hence the measured relative CIAG dips $D_{v''}(v')$ for a range of v'' levels yield the relative cross sections $\sigma_{A, v''}(v')$ as a function of v'' , i.e., the branching ratios. The distribution of $[A, v'']$ from Refs. 23 and 33 is close to an exponential, decreasing by $\approx 20\%$ in going to the next higher v'' level in the range of interest. Because these measurements did not cover all v'' levels relevant to this work, the original data were fitted and extrapolated using the distribution

$$P(v'') \approx \exp[-G(v'')/4776 \text{ cm}^{-1}], \quad (8)$$

where $G(v'')$ is the $N_2(A)$ vibrational term value.

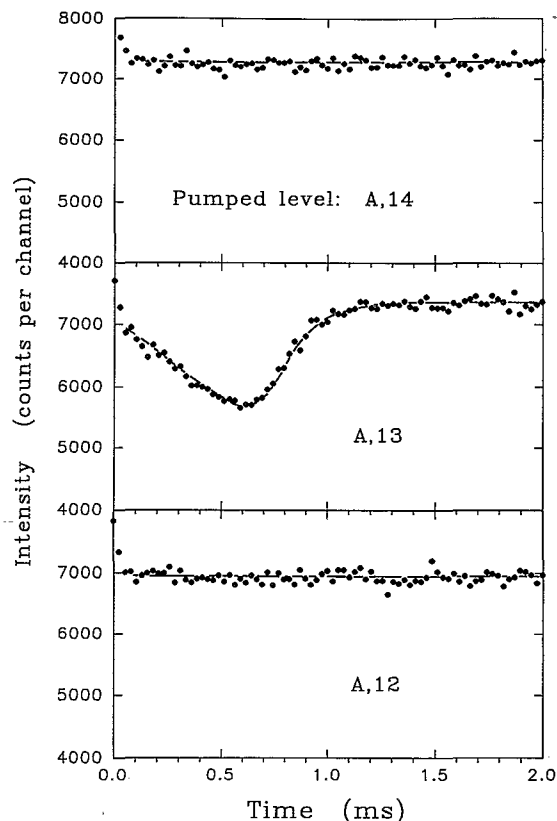


FIG. 4. CIAG emission from $B, v'=4$, after laser depletion at $t=0$ of the three A, v'' levels indicated (in each case pumped via the $\Delta v=5$ transition). Only the near-resonant $v''=13$ level (cf. Fig. 1) produces a CIAG dip. The collision gas was argon.

Figure 4 gives typical results on the collisional energy transfer to the level $B, v'=4$ from the levels $A, v''=12, 13$, and 14 . As seen in Fig. 1, the $B, 4$ level is in close resonance with $A, 13$. Accordingly, the middle panel of Fig. 7 shows a large CIAG dip in the $v'=4$ emission upon pumping of the $v''=13$ level. On the other hand, pumping the off-resonance levels $v''=12$ and 14 has no effect on the CIAG intensity within the error limits. Thus the adjacent v'' levels contribute less than 3% relative to the dominant, resonant level in this case.

A very similar situation obtains in the group of levels $B, v'=6/A, v''=15, 16$, and 17 . The CIAG dip for the resonant case $A, 16$, has already been shown in Fig. 3. Pumping of the two other v'' levels yielded no discernible CIAG dip.

By contrast, Fig. 5 illustrates a case where the product level, $B, v'=7$, lies about midway between two potential reactant levels, $A, v''=17$ and $A, v''=18$. The very exothermic transfer $A, 19 \rightarrow B, 7$ (top panel) evidently does not take place. The two CIAG dips for $v''=17$ and 18 are in the ratio of 1:4.5, which is, in this example, essentially equal to the ratio of $\sigma_{A, 17}(7) \cdot [A, 17] : \sigma_{A, 18}(7) \cdot [A, 18] = 1:4.5$ [cf. Eqs. (6) and (7)]. With the relative population $[A, 17] : [A, 18] = 1:0.82$ from Eq. (8) one then finds the branching ratio $\sigma_{A, 17}(7) : \sigma_{A, 18}(7) = 1:5.7$ (cf. the corresponding two absolute cross sections 0.6 and 3.4 \AA^2 in

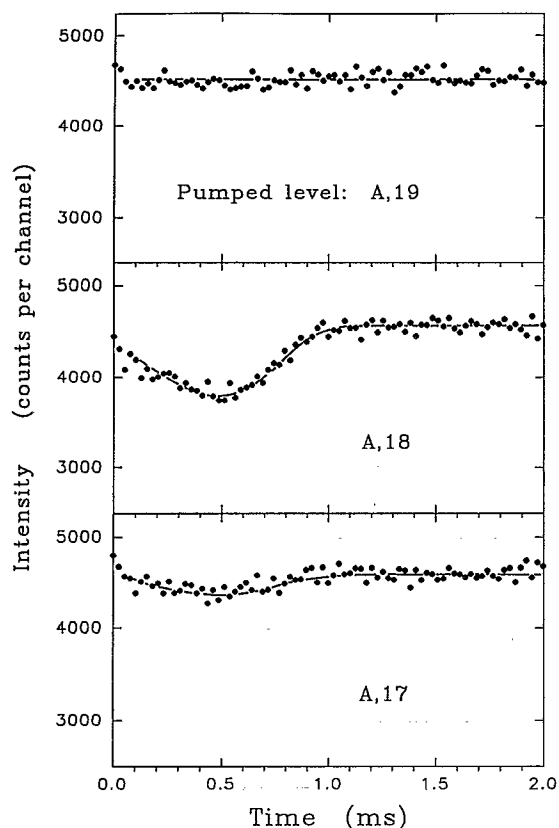


FIG. 5. Same as Fig. 4, but for $B, v'=7$, and pumping of $A, v''=17, 18, 19$, collision gas krypton. The relative CIAG dips in the two lower panels yield the cross section branching ratio for the $A, 17 \rightarrow B, 7$ and $A, 18 \rightarrow B, 7$ energy transfer, see the text.

Table III for Kr, which were derived from this branching ratio as described in the following section).

In the same manner pathways for the collisional population of the entire range of levels $B, v'=4-10$ were explored, in each case with the collision gases Ar, Kr, Xe, N_2 , and H_2 . For the levels $v'=6$ and 7 , O_2 and NO were also used. The pressure of the collision gas during the experiments was maintained around $3 \cdot 10^{-3}$ mbar, which gives a CIAG intensity close to (or below) its maximum, see Ref. 19. Accurate measurements made for $B, 4$, $B, 6$, and $B, 7$ using several collision gases show no pressure dependence of the relative CIAG dip, $D_{v''}(v')$, in the range of $0.5-10 \cdot 10^{-3}$ mbar. This indicates that any secondary processes are negligible. The experimental errors limited the determination of branching ratios to $>1:10$ to $1:20$. All measured branching ratios were corrected for the small impurities of the laser excitation by overlap with the adjacent bands (see Appendix C). The consistent conclusion from all these experiments was that energy resonance plays indeed the crucial role in the process of $N_2(A-B)$ collision-induced intramolecular energy transfer. Quantitative results on the branching ratios are given below in the form of the state-to-state absolute cross sections (Table III).

The magnitude of $D_{v''}(v')$, the relative CIAG dip, was in most cases only weakly dependent on the collision gas, although the CIAG intensities themselves vary strongly with the collision partner.¹⁹ Especially in the case of reso-

nant levels (v', v'') the values of $D_{v''}(v')$ measured with different collision gases were, in fact, the same within experimental error. This follows from Eq. (6), where a near-resonant cross section $\sigma_{A, v''}(v')$ will be dominant in the denominator, and cancels out. Important exceptions are, however, the collisions with Xe and NO, where the values of $D_{v''}(v')$ were found to be systematically smaller by about 20%-30% than for the other gases. This is an indication of significant contributions from channels other than the $A, v'' \rightarrow B, v'$ transfer, such as are summarized in the term $Z_{v''}$ in Eq. (6), and tend to reduce the measured CIAG dip. These additional processes could be collision-induced intramolecular transitions from the metastable singlet species $N_2(a$ and $a')$ which are also present in the beam. In the case of heavy target particles such as Xe, spin orbit interaction is strong and can induce singlet-triplet collision-induced transitions. For NO, having a $^2\Pi$ ground state, singlet-triplet transitions are allowed by the correlation rules.

C. Absolute cross sections

In Ref. 19, only relative data could be obtained for the efficiency of the collisional $A, v'' \rightarrow B, v'$ coupling. If absolute cross sections can be measured for at least one of these processes, then the entire body of data can be referred to an absolute scale. This is indeed possible. From Eq. (4) it is seen that the cross section $\sigma_{A, v''}(v')$ is proportional to the ratio $\Delta I_{v'}/\Delta[A, v'']$. $\Delta[A, v'']$ is in turn proportional to the intensity of the fluorescence induced by the depopulating laser pulse. Therefore $\sigma_{A, v''}(v')$ is proportional to $\Delta I_{v'}/I_{LIF}$

$$\sigma_{A, v''}(v') = K \cdot \Delta I_{v'}/I_{LIF}. \quad (9)$$

The proportionality constant K contains only well-determined experimental parameters [see Appendix D, Eq. (D1)]. The exact meaning of the quantity $\Delta I_{v'}$ within the time-dependent CIAG dip curve is specified in Appendix D. Finally, I_{LIF} designates the time integral from $t=0$ over the entire laser-induced fluorescence signal, and is also discussed in Appendix D. For the calibration experiment the optical pumping scheme illustrated in Fig. 6 was used. The cross section to be measured is for the well-resonant transition $A, 13 \rightarrow B, 4$ (cf. Fig. 4), employing detection of the CIAG on the $(4, 2)$ band at 750 nm, and $\Delta v=5$ pumping on the $B, 18 \leftarrow A, 13$ transition (518 nm) as before. In addition, LIF emission is now observed on the $(18, 17)$ band at 653 nm.

Absolute cross section measurements following this scheme were made for $M=Ne, Ar, Kr, Xe, H_2$, and N_2 . In order to ensure that the data are not affected by the scattering of the beam molecules before reaching the observation region, measurements were performed at different target gas pressures between $0.5 \cdot 10^{-3}$ and $2 \cdot 10^{-3}$ mbar. The results from Eq. (D1) were then extrapolated to zero pressure to obtain the true cross section. At 10^{-3} mbar this correction amounted to at most 15%. The final absolute state-specific cross sections for the $A, 13 \rightarrow B, 4$ transition are given in the first line of Table II. They serve to calibrate all other data as follows.

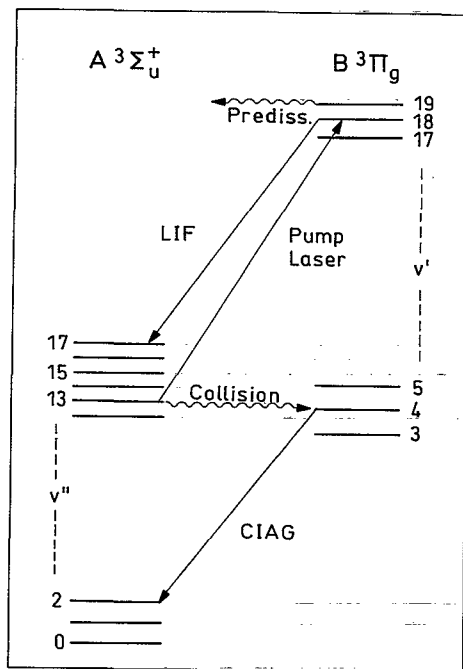


FIG. 6. Scheme of the absolute cross section measurement. Portions of the *A* and *B* state vibrational ladders are shown. The near-resonant transfer $v''=13 \rightarrow v'=4$ is induced by collisions with Ne, Ar, Kr, Xe, H₂, and N₂. $\Delta v=5$ pumping of $v''=13$ causes dips in the (4,2) CIAG emissions. Subsequently the (18,17) LIF signal was measured, with the photomultiplier repositioned (Fig. 2). After correction for predissociation (Fig. 16) its intensity, relative to that of the CIAG dip (at $t=100 \mu\text{s}$, see the text) yields the absolute cross sections.

In the second line of Table II, the corresponding relative cross sections for the transfer to *B*, $v'=4$ are listed, as measured in Ref. 19 and given graphically in Figs. 11(a) and 11(b) of that work. The present branching ratio measurements (see Table III below) show that these earlier data are essentially also pure state-to-state cross sections for the (near-resonant) *A*, $13 \rightarrow B$, 4 channel. Only for Xe and N₂ additional, weak transitions were observed from $v''=14$ and 15, respectively, which make contributions of 12% (from the branching ratios and the relative *A*-state level populations). With these corrections, state-specific *A*, $13 \rightarrow B$, 4 relative cross sections are obtained as given in Table II, line 3. The ratios γ of these values and σ_{abs} from line 1 are given in the last line.

TABLE II. Absolute and relative cross sections.

	Ne	Ar	Kr	Xe	H ₂	N ₂
$\sigma_{\text{abs}}(\text{\AA}^2)^a$	0.47	2.2	3.7	7.1	0.46	2.5
σ_{rel}^b	(398.0) ^c	7155.0	16256.0	45476.0	1775.0	9760.0
$\sigma_{\text{rel}}^d(\text{corr})$	(398.0)	7155.0	16256.0	39428.0	1775.0	8462.0
γ^e	(847.0)	3252.0	4394.0	5553.0	3859.0	3385.0

^aMeasured for the transition *A*, $13 \rightarrow B$, 4 see the text.

^bFrom Ref. 19, cf. Fig. 11 of that work, for the total population of *B*, 4.

^cThe Ne data from Ref. 19 are probably too small by a factor of 4.5. The CIAG signal is very small for Ne, and comparable to the AG background, which is especially large for low *B*, v' levels such as *B*, 4 [cf. Ref. 19, Fig. 4(a)]. In addition, part of the CIAG signal is not due to *A* \rightarrow *B*, but to *W* \rightarrow *B* transfer.

^dRelative cross section for *A*, $13 \rightarrow B$, 4 only, corrected for additional branches in the case of Xe and N₂.

^e $\gamma = \sigma_{\text{rel}}(\text{corr.})/\sigma_{\text{abs}}$.

Ideally, γ should be the same for each gas. However, with Ne the CIAG signal is so weak that the σ_{rel} data are quite unreliable, and $\gamma(\text{Ne})$ is meaningless. $\gamma(\text{Xe})$ appears to be too large compared to the remaining γ 's; possibly further, unrecognized reaction channels contribute here to σ_{rel} , see above. The other four γ values, however, are remarkably similar, considering that they are based on CIAG cross sections measured by two totally different techniques and spanning a range, from H₂ to Kr, of 1 order of magnitude. $\gamma(\text{Ar}, \text{Kr}, \text{H}_2, \text{N}_2)$ lie within 12% standard deviation of their mean, $\bar{\gamma}=3722$, which was then used to calibrate the σ_{rel} values for the other transitions.

In very resonant cases this normalization is straightforward. Whenever the measurements indicated a negligible contribution of the non-resonant channels, σ_{rel} from Ref. 19 could safely be ascribed solely to the resonant pathway, and the absolute cross section was then obtained simply as

$$\sigma_{\text{abs}} = \sigma_{\text{rel}}/\bar{\gamma}. \quad (10)$$

An example is the $v''=16 \rightarrow v'=6$ transfer, where for Ar, H₂, N₂, NO, and O₂ no other channels populating $v'=6$ were found, cf. Table III. For He and Ne no measurements of branching ratios were attempted because of the low CIAG intensity, but the other observations show that non-resonant processes become very weak for the light collision gases. Therefore, it is justified to calculate the absolute cross sections for He and Ne, for all $v'' \rightarrow v'$ transitions, according to Eq. (10). If more than one level contributes, the respective cross sections were obtained as described in Appendix E.

The final compilation of the absolute cross sections for all levels and gases studied is given in Table III. The data are also presented in graphical form in Fig. 7, as a semilog plot of the cross sections vs the absolute energy mismatch, $|\Delta E|$, between the reactant and product level. This type of plot facilitates the comparison with an energy dependence of the cross section as predicted by the "exponential gap law",¹⁹

$$\sigma = \sigma_0 \cdot \exp(-|\Delta E|/E_0), \quad (11)$$

see below. The overall appearance of Fig. 7 is similar to the analogous Fig. 11 in Ref. 19, except that there are now considerably more data points. The earlier work yielded only a single, effective cross section for each *B*, v' level, i.e.,

TABLE III. Cross sections (in Å²) for collision-induced intramolecular transitions N₂(*A*, *v*'' → *B*, *v*').

<i>B</i> , <i>v</i> '	<i>A</i> , <i>v</i> ''	Δ <i>E</i> ^a cm ⁻¹	He ^b	Ne ^b	Ar	Kr	Xe	H ₂	N ₂	NO ^b	O ₂ ^c
4	12	-864			<0.1	<0.2	<0.3	<0.02	<0.01		
4	13	223	0.1 ^e	0.47 ^d	2.2 ^d	3.7 ^d	7.1 ^d	0.46 ^d	2.5 ^d	6.0	
4	14	1279			<0.1	<0.4	1.3	<0.04	<0.3		
4	15	2303							0.6 ^f		
5	14	-310			0.12	0.42	4.2	0.09	0.20		
5	15	713	0.03 ^e	0.06 ^e	0.28	0.68	3.7	0.22	0.19	4.0	
5	17	2556							0.28 ^f		
6	15	-847			<0.1	<0.2	<0.5	<0.04	<0.2	<0.5	<0.3
6	16	142	0.25	0.53	2.8	4.2	10.4	1.2	3.7	9.7	2.8
6	17	1096			<0.2	0.45	2.8	<0.06	<0.3	<0.7	<0.3
7	17	-435			<0.07	0.6	2.2	0.10	0.12	1.3	0.2
7	18	483	0.11	0.23	1.3	3.4	8.0	0.48	1.1	4.3	1.5
7	19	1363			<0.1	<0.2	<0.1	0.1	0.15	1.1	<0.1
8	19	-139	0.10	0.15	0.47	1.5	7.5	0.5	0.82	6.6	
8	20	700			0.58	1.7	3.2	0.3	0.35		
9	20	-772			<0.1	<0.4	<1	<0.06	<0.1		
9	21	26	0.19	0.34	1.8	5.1	15.5	1.0	2.2	9.9	
9	22	779			0.5	0.9	<1.0	0.3	0.6		
10	22	-669			<0.3	<0.6	<2.0		<0.5		
10	23	41	0.6 ^g	0.9 ^g	4.0	7.4	18.0	3.8	4.2	15.0	
<i>E</i> _{c.m.} , cm ⁻¹			400.0	625.0	750.0	870.0	925.0	360.0	685.0	700.0	710.0
<i>v</i> _{rel} , m/s			1660.0	1130.0	1045.0	1000.0	980.0	2150.0	1080.0	1075.0	1065.0

^aΔ*E* is the energy difference between the *v*', *v*'' levels indicated, in cm⁻¹. Negative Δ*E* corresponds to endoergic transitions.

^bFor He, Ne and, with the exception of *B*, *v*'=6 and 7, for NO, branching ratios were not measured.

^cAbsolute cross sections were obtained by normalization to N₂ from the ratio of the dip magnitudes (in counts) measured for O₂ and for N₂ at equal pressure.

^dDirectly measured absolute cross sections, from Table II.

^eFor reasons explained in footnote c of Table II, the *A* → *B* transfer fraction of the total signal could not be reliably determined. It was assumed to have the same value (85% for *v*'=4, 68% for *v*'=5) as measured for Ar.

^fNot included in Fig. 7.

^gSee Note added in proof.

seven or eight data points in Fig. 11 of Ref. 19. In the present work the branching ratio measurements have made it possible to partition most of these cross sections into two or three *A*, *v*'' contributions, resulting in a total of up to 12 data points for many gases in the present Fig. 7. For instance, there are now two cross sections for Kr, *v*'=6, represented in the Kr panel of Fig. 7 by the third-highest and the lowest dot (cf. Table III).

Note that the experimental uncertainty of the vibrational energy of high-lying levels *v*', *v*'' and hence of the energy balance |Δ*E*| is greater than for the low levels. This is discussed in Appendix F.

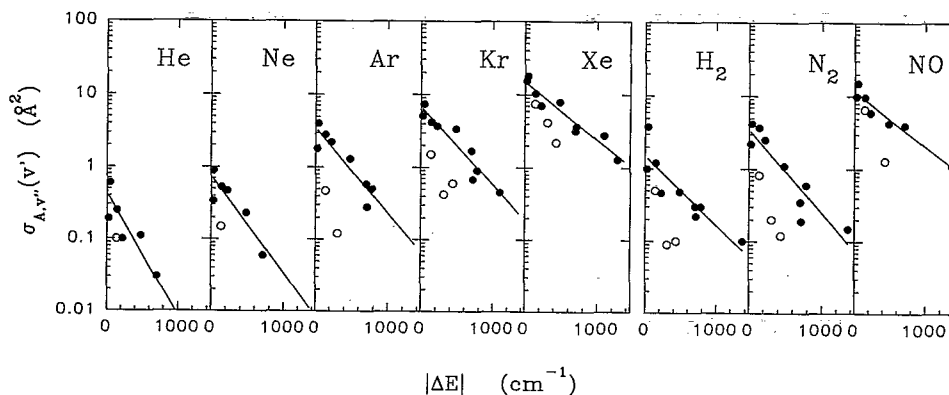


FIG. 7. Absolute state-to-state cross sections for collision-induced intramolecular energy transfer N₂(*A*, *v*'' → *B*, *v*') measured for the collision gases indicated, and plotted vs the energy gap |Δ*E*| between reactant and product levels. Circles mark endothermic, dots exothermic processes. The straight lines are least-squares fits through the exothermic data points only.

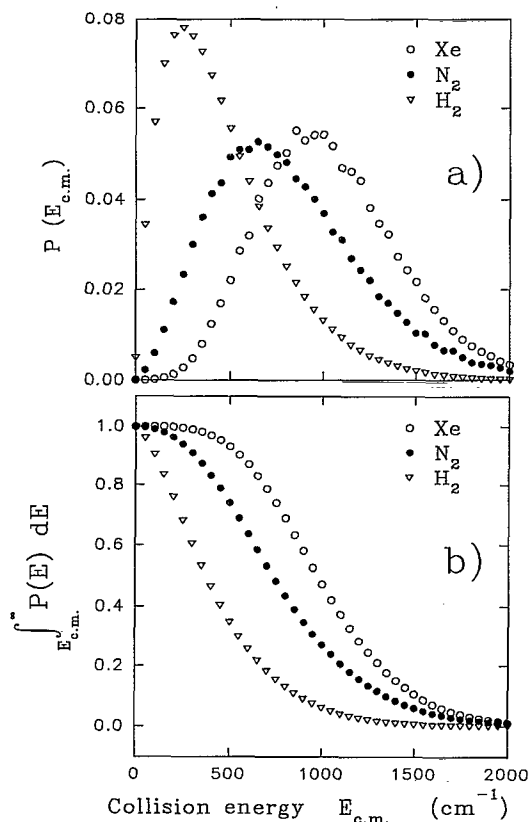


FIG. 8. (a) Distribution functions of relative collision energy of $\text{N}_2(A)$ in the beam vs room temperature random targets of the three gases indicated. (b) Percentile plot of the distributions shown in (a).

IV. DISCUSSION

A. Endothermic versus exothermic processes

Figure 7 brings out the fact that the cross sections for endothermic transitions, represented by open circles, are generally much smaller than those of exothermic processes (dots) with similar $|\Delta E|$. It is important to realize that this is not simply due to the fact that for the former the mean collision energy may barely be sufficient to overcome the endothermicity threshold. Figure 8(a) shows the distribution of the relative collision energies in this experiment for three gases. The curves were calculated numerically for the measured velocity distribution of the N_2 beam²³ and the random room-temperature Maxwellian distributions of the target gases. The corresponding mean relative collision energies are given at the bottom of Table III. For a comparison with the endothermicities, Fig. 8(b) is especially informative. It shows the fraction of collisions with an energy greater than a given value. For example, for $\Delta E = -435 \text{ cm}^{-1}$ ($v''=17 \rightarrow v'=7$), 41% of all H_2 collisions and 95% of all Xe collisions have energies greater than this threshold. Yet the corresponding H_2 cross section (0.10 \AA^2 , Table II) is only 21% of the exothermic $v''=18 \rightarrow v'=7$ cross section for a similar $|\Delta E|$. In a rough approximation one could “correct” the endothermic H_2 cross section by normalizing it to the 41% “effective” collisions, but even then it is still too small by a factor of two.

It is true that this “correction” assumes a step function behaviour of the cross section at the threshold, and any more realistic, smoother increase will make the correction factor greater. However, Fig. 7 also shows many examples of the endothermic cross sections being much smaller than the exothermic ones at a comparable ΔE even for heavy gases and small ΔE , where the threshold effects are minimal. Therefore, it appears that the reaction mechanism itself favors the exothermic channels, by the details of the interaction potentials (see below).

It is not unlikely that this is also true for the $\text{N}_2(W, v) \rightarrow \text{N}_2(B, v')$ collisional energy transfer studied in Ref. 19. Without any possibility of labeling the $\text{N}_2(W)$ vibrational levels by laser pumping, the assignment of the dominant reaction path is here somewhat speculative. In Ref. 19, that $\text{N}_2(W)$ level was taken to be responsible for the population of a given v' level which was nearest-to-resonance, irrespective of the sign of ΔE . In the light of the present results this conclusion very likely remains valid for the levels $v'=4$ through 8: For $v'=4, 5$, and 6 the nearest-to-resonance transition is exothermic and is therefore perhaps basically favored as in the $A \rightarrow B$ transfer; and for $v'=7$ and 8 the near-resonant channel, although slightly endothermic, is probably much more important than the corresponding exothermic channel which is very far off-resonance. Only the cases $v'=3$ and 9 are ambiguous, with possible contributions from a strongly endothermic and an even more off-resonance exothermic channel. Accordingly these cross sections are among the smallest for each gas, and were in Table II of Ref. 19 ascribed to the pairs of W -state levels $v=3$ and 4 (for $v'=3$) and $v=10$ and 11 (for $v'=9$). In Fig. 12 of Ref. 19, however, the $v'=3$ and 9 cross sections were attributed to the endothermic channel only, because it has the somewhat smaller $|\Delta E|$ ($\Delta E = -583$ and -516 cm^{-1} , respectively). This may have to be revised if the $W \rightarrow B$ transfer resembles the $A \rightarrow B$ process. Figure 9 shows a modified version of Fig. 11 in Ref. 19, where the $v'=3$ and 9 relative cross sections have now been plotted at the ΔE of the corresponding exothermic channel ($\Delta E = 824$ and 721 cm^{-1} , respectively). They have also been renormalized to the slightly smaller populations $[W, v]$ of the pertinent reactant levels. This new plot facilitates at the same time the comparison with the present Fig. 7, in the same format for the $A \rightarrow B$ transfer.

B. Comparison with exponential gap law

The straight lines shown in Figs. 7 and 9 were obtained by a fit to the $\ln(\sigma)$ data points [a fit of the exponential, Eq. (11), to the σ values themselves gives similar results]. For the $A \rightarrow B$ transfer, only the exothermic channels (filled dots) were included in the fit, because there is strong evidence that the endothermic reactions occupy a special position (see above). This is an important difference to the otherwise similar fit procedure in Ref. 19. Also now, of course, absolute rather than relative cross sections for $A \rightarrow B$ transfer have been fitted. In the case of $W \rightarrow B$ transfer, Fig. 9, the only change from Ref. 19 is the shift of the $v'=3$ and $v'=9$ data points (see above). The two remain-

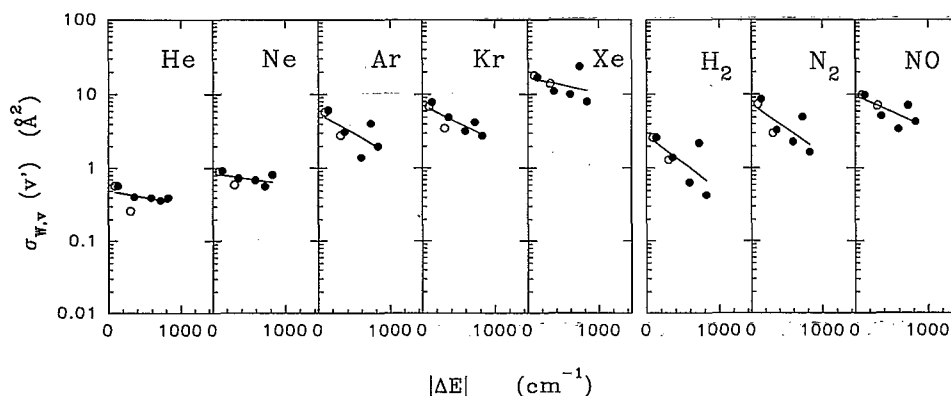


FIG. 9. Same as Fig. 7, for $N_2(W \rightarrow B)$ collision-induced energy transfer. Results are from Ref. 19, although in each panel two data points have been replotted, based on analogies with the present $A \rightarrow B$ transfer results. Unlike Fig. 7, the cross sections are only approximately state-to-state (see the text), and the straight line fits include here the endothermic processes.

ing endothermic channels, for $v' = 7$ and 8, are quite close to resonance and probably do contribute significantly, since they merge smoothly with the exothermic points in Fig. 9. These two endothermic cross sections were therefore included in the overall fit in this case, for want of any branching ratio data.

As in the earlier work,¹⁹ the exponential gap law, Eq. (11), is seen to provide a reasonably good overall description of the cross section dependence on ΔE . The parameters σ_0 and E_0 resulting from the data fits are collected in Table IV. It can be compared with Table III of Ref. 19. For the $W \rightarrow B$ transition σ_0 is now smaller by 22% (averaged over the eight collision partners), while E_0 is larger by factors of 2.4 ± 0.8 . Both of these differences derive directly from the displacement of two data points discussed above. For the $A \rightarrow B$ transfer, σ_0 can only be compared with the relative values in Ref. 19. The dependence on M is quite similar, the deviations lying within $\pm 10\%$ on average. For E_0 again a significant difference with the previous results is found. Separating the exothermic and endothermic contributions by means of the measured branching ratios has here yielded values of E_0 (now for the exothermic channels only) which are larger by factors of 3.8 ± 0.8 than in Ref. 19, and are less dependent on the collision partner. Basically the earlier analysis had overemphasized the endothermic channels. Thus for both reactions the resonance condition is less stringent than was suggested by the data of Ref. 19. It is still true, however, that E_0 is considerably smaller for $A \rightarrow B$ than for $W \rightarrow B$ transfer (averaged over all collision partners, $E_0 \approx 420 \text{ cm}^{-1}$ vs

1180 cm^{-1} , respectively). As was already remarked in Ref. 19, this finding is surprising in view of the identical electron configuration of the A and W states.

In Ref. 19 a pronounced increase of the $A \rightarrow B$ cross sections for a given B, v' level in the order $\text{He} \cdots \text{Xe}$ and $\text{H}_2 \cdots \text{NO}$ was found. In fact, phenomenologically this increase was roughly quasi-“exponential,” since in Fig. 11 of Ref. 19 corresponding $\sigma_A(v')$ data points fall almost on an ascending straight line across the “M” panels. This behavior is again found for the state-to-state $A \rightarrow B$ cross sections measured in this work. In the present Fig. 7, corresponding $\sigma_A(v')$ points can be identified by their ΔE , and connecting them for different M yields roughly a common straight line for each v' level.

It is important to note that in this work the exponential gap law is used in the form of Eq. (11) with an adjustable parameter E_0 , rather than the expression $\exp(-|\Delta E|/kT)$ proposed in Ref. 34. In fact the experimental observations^{35–38} made for different molecules could not confirm the validity of the latter. No conclusions can be drawn from the present measurements of the $A \rightarrow B$ and $W \rightarrow B$ couplings as to the widely postulated FCF dependence of the cross sections,^{15,34–41} because the FCF for the transitions of interest depend only slightly on the initial vibrational level A, v'' or W, v .

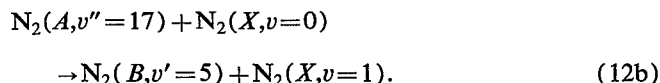
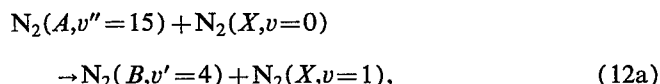
The $A, v'' \rightarrow B, v'$ cross sections listed in Table III include two cases of seemingly far off-resonance energy transfer, $v'' = 15 \rightarrow v' = 4$ and $v'' = 17 \rightarrow v' = 5$, in both cases with N_2 as a collision partner. The nominal exothermicities, $\Delta E = 2303$ and 2556 cm^{-1} , are so large that these data

TABLE IV. Characteristic cross sections σ_0 (in \AA^2) and energy gap parameters E_0 (in cm^{-1})^a for $W \rightarrow B$ and $A \rightarrow B$ transfer.

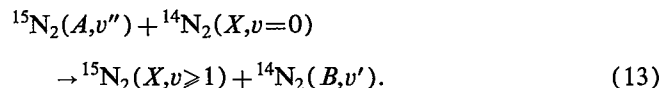
M	He	Ne	Ar	Kr	Xe	H ₂	N ₂	NO
$W, v \rightarrow B, v'$								
σ_0	0.50	0.84	5.6	7.2	17.0	2.8	7.4	9.7
E_0	2270.0	3280.0	780.0	890.0	1970.0	580.0	655.0	985.0
$A, v'' \rightarrow B, v'$								
σ_0	0.35	0.74	3.47	6.79	15.0	1.47	3.5	11.7
E_0	310.0	325.0	370.0	405.0	550.0	460.0	380.0	580.0

^aDefined in Eq. (11).

points were not included in Fig. 7. The collision-induced transitions $v''=14 \rightarrow v'=4$ and $v''=16 \rightarrow v'=5$, although closer to resonance by 1024 and 854 cm^{-1} , respectively, were not observed. The explanation for this unusual behavior is a process whereby most of the excess energy is taken up in vibrational excitation of the target N_2 molecule from $v=0$ to $v=1$



The vibrational quantum of N_2 is $\Delta G_{1/2} = 2330 \text{ cm}^{-1}$, which makes reaction (12a) endothermic by 27 cm^{-1} and reaction (12b) exothermic by 226 cm^{-1} , both now close to resonance. With N_2 as a collision partner it is not possible to decide whether the observed $\text{N}_2(A \rightarrow B)$ transfer is intramolecular, like in all other cases, or intermolecular. In fact, experiments in a nitrogen afterglow with isotopic substitution have shown that the intermolecular electronic energy transfer is an important mechanism.⁴² It is then usually accompanied by vibrational excitation of the electronic ground state product

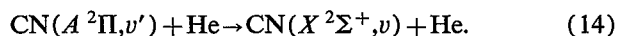


In the present work, only two examples of this mechanism were found. This type of process can best be observed for the lowest v' levels. For larger v' , the population of the required rather high reactant A, v'' levels in the beam becomes too low. For the same reason a corresponding process with H_2 , having the much larger $\Delta G_{1/2} = 4159 \text{ cm}^{-1}$, is less likely to be observable, although a systematic search with the other molecular target gases was not made.

C. Electronic structure

In this work and in Ref. 19 collision-induced transitions from N_2 reactant state of “ungerade” electron inversion symmetry, $A^3\Sigma_u^+$ and $W^3\Delta_u$, to a “gerade” state, $B^3\Pi_g$, have been studied. Coupling between these states is only possible in the vicinity of a third particle which breaks the overall electronic symmetry. Thus we expect that the process studied here will take place in the repulsive region of the interaction potentials.

This view is supported by *ab initio*⁴³ and quantum scattering⁴⁴ calculations on the closely related process



Corresponding experimental studies, except with Ar instead of He, showed that the close-to-resonance product levels v are populated, similar to our findings. The calculations demonstrated very clearly how the $\text{CN}(A \rightarrow X)$ coupling increases dramatically in the repulsive branch.

The analogy of the CN and the N_2 systems is in fact quite close. A comparison of the electronic configurations shows this. Both the N_2 A and W states have the leading

configuration $\cdots \pi_u^3 \sigma_g^2 \pi_g$, while $\text{N}_2(B)$ is $\cdots \pi_u^4 \sigma_g \pi_g$.⁴⁵ Thus the energy transfer is effected by the transformation of a single electron, $\sigma_g \rightarrow \pi_u$. With CN, the configurations of the A and X states are, respectively $\cdots 1\pi^3 5\sigma^2$ and $\cdots 1\pi^4 5\sigma$, and again the transition corresponds to a $5\sigma \rightarrow 1\pi$ electron change. In fact, the correspondence between the $\pi_u/1\pi$ and the $\sigma_g/5\sigma$ orbitals is semiquantitative, since CN was shown in the calculations⁴³ to behave almost like a homonuclear molecule. There is also experimental evidence for this: The $A \rightarrow X$ energy transfer in CN (Refs. 34,35) and the corresponding $A^2\Pi_u \rightarrow X^2\Sigma_g^+$ transfer in the isoelectronic, but truly homonuclear N_2^+ species^{36,37} show very similar features.

Therefore, we can assume that many of the results of the CN*-He calculations are applicable to the present $\text{N}_2^*\text{-M}$ systems also. In particular we propose that even for the heavier species M the critical interaction region is in the repulsive branch. This is strongly suggested by the overall similarity of the trends of the cross sections with $|\Delta E|$ for light and heavy collisional partners as exhibited in Figs. 7 and 9. If, for the heavy species M, an additional mechanism via the attractive potential became operative, then this would very likely show up in the form of a switch to a different ΔE dependence. In a crude reaction model we ignore, therefore, the long-range attractive potentials, although the depth of the van der Waals potential for, e.g., Kr or Xe, will certainly be much larger [110–140 cm^{-1} (Refs. 46–48)] compared to $\approx 10 \text{ cm}^{-1}$ well depth calculated for CN-He.⁴³

From the premise of essentially only repulsive interactions and the observation that exothermic processes are fundamentally favored over endothermic ones, a rough conclusion about the relative curvature of the entrance and exit channel potentials can be drawn. If the former become repulsive at shorter range than the latter, then potential crossings will exist for the exothermic, but not for the endothermic vibrational levels. This is illustrated in the schematic Fig. 10. Figure 10(a) shows the exit, $\text{N}_2(B, v') + \text{M}$ potential for a given v' , along with entrance potentials $\text{N}_2(A, v'') + \text{M}$ for several v'' . These are assumed identical in shape, but displaced against each other by the v'' vibrational spacing, in the spirit of the Bauer-Fisher-Gilmore model.⁴⁹ Strong support for the independence of the potential on the vibrational excitation comes again from the CN-He calculations (Ref. 43, Fig. 1, although here with respect to the θ , rather than R , coordinate).

In Fig. 10(a) the entrance and exit potentials are assumed to be not very different in shape, and this results in a high selectivity for near resonant processes: If in Fig. 10(a) a larger value for ΔE is assumed, then the crossing point will lie too high to be energetically accessible. The $\text{N}_2(A \rightarrow B)$ transfer could be of this type. The $\text{N}_2(W \rightarrow B)$ transfer, on the other hand, is distinctly less resonance-selective than the $\text{N}_2(A \rightarrow B)$ transfer. This can be modeled by assuming a somewhat flatter shape of the $\text{N}_2(W) + \text{M}$ potential, so that here even with a substantial ΔE , an accessible crossing point will still exist [Fig. 10(b)]. The differences between the shapes of the potentials are not expected to be very large, because the outermost orbital (π_g)

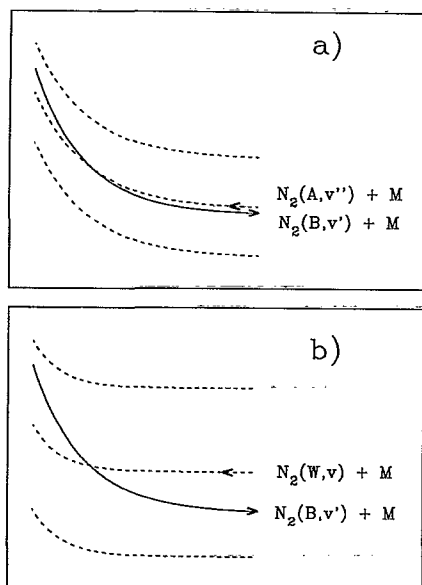


FIG. 10. Schematic interaction potentials $N_2(A, B, W) + M$. The exit potentials $N_2(B, v') + M$, identical in (a) and (b), are crossed by entrance potentials $N_2(A, v'') + M$ and $N_2(W, v) + M$ for exothermic processes. The $N_2(A, v'') + M$ potentials in panel (a) are assumed very similar in shape to the exit potentials, allowing only close-to-resonance processes (Fig. 7). The $N_2(W, v) + M$ potentials, panel (b), are assumed flatter, to allow processes with larger ΔE to contribute in accordance with the observation, Fig. 9.

is the same in all three states involved, and the different occupation of the π_u and σ_g orbitals will be somewhat shielded in the long-range behavior. Nevertheless, it can be anticipated from density plots of these two orbitals⁵⁰ that the $\pi_u^4\sigma_g^2$ configuration is somewhat more repulsive than the $\pi_u^3\sigma_g^3$ configuration for the sideways approach, because the π_u orbital extends much further from the molecular axis than the σ_g orbital. This qualitative prediction is also borne out by the CN-He calculations (Figs. 2–4 in Ref. 43). Thus the postulated slightly greater long-range repulsion of the exit channel $N_2(B) - M$ can be rationalized. The difference between the two entrance channel potentials, $N_2(A) - M$ and $N_2(W) - M$, is expected to be even more subtle in origin and is difficult to predict.

The intramolecular nonadiabatic transitions are known to take place in the vicinity of crossing “seams” between the entrance and exit potential energy surfaces. For the CN-He system this has been demonstrated by explicit calculations of the coupling matrix elements.⁴³ They were found to be large only at CN bond lengths close to the crossing point of the $A^2\Pi$ and $X^2\Sigma^+$ potentials of isolated CN. Moreover, the quasis resonant ($A, v=7$ and 8)/($X, v=11$ and 12) levels that were studied experimentally in Refs. 34 and 35 have classical outer turning points which are located close to this seam. This enforces a good overlap of the corresponding vibrational wave functions. The Franck-Condon condition of minimal kinetic energy change is also at this point automatically fulfilled for a pair of quasis resonant levels. Consequently, near-resonant transitions are strongly favored.

A very similar condition exists for $N_2(A \rightarrow B)$ transfer.

The corresponding potential curves of the N_2 molecule cross at 1.07 \AA (in this case on the inner limb), and this point forms the onset of a crossing seam of the corresponding potential surfaces of the triatomic collision system. Moreover, because the $N_2(A)$ and $N_2(B)$ curves are almost tangent to each other, the seam is essentially not a line, but a wide band, which happens to encompass just the region of the A, v'' and B, v' levels studied here (from about 8 to 9 eV above the $N_2(X)$ ground state). Thus the analogy between the $CN(A \rightarrow X)$ and the $N_2(A \rightarrow B)$ transfer is very close. In both cases the location of the seam near the classical turning points of the initial and final state vibrational levels favors the quasis resonant transitions, because the corresponding wave functions are large at this point, and the kinetic energy change is small.

For the $N_2(W \rightarrow B)$ transition, on the other hand, the topology of the surface crossings is quite different. For the isolated N_2 molecule, the W -state potential curve intersects that of the B state near its minimum, far away from the classical turning points of the coupled near-resonant vibrational levels. Thus a favorable wave function overlap in the critical region will in this case not automatically exist. Nevertheless, the Franck-Condon factors for comparable pairs of levels are, in fact, three to ten times greater in the $W \rightarrow B$ case than for $A \rightarrow B$ (see Table IV of Ref. 19). This is the result of the similar shape of the $N_2 B$ and W potentials, with only a slight radial shift between them. Thus the less favorable conditions for $N_2(W \rightarrow B)$ transfer at the crossing seam itself are compensated by the larger vibrationally averaged transition probability. This may explain why the overall magnitude of the cross section for $N_2(A \rightarrow B)$ and $N_2(W \rightarrow B)$, for the same collision partner, is quite similar.

In a full treatment of the intramolecular energy transfer between the N_2 triplet states one should, in principle, also consider the coupling between the A and W states, because crossings among the corresponding potential surfaces may also act as intermediary steps in the $A \rightarrow B$ and $W \rightarrow B$ transfer studied. An additional complication could arise from the $B' \ ^3\Sigma_u^-$ state which also lies in the region of interest and has relevant crossing seams with the B state. In fact, population of the B' state by energy transfer from the B state or other triplet states has experimentally been observed.^{3,4,14} Thus with N_2 up to four triplet states can mutually interact, while in the CN case only two states need to be considered.

D. Comparison with previous work

Up until about 15 years ago no truly state selective studies of $N_2(A \rightarrow B)$ transfer were made. After pioneering work of Heidner *et al.*¹⁰ using laser techniques for the first time in 1976, subsequent related work by Sadeghi and Setser^{11,15} as well as by Rosenwaks and co-workers^{12,16} has produced a wealth of kinetic data. Thanks to the high energy and time resolution offered by laser excitation, perfect initial state preparation was achieved. The investigation most similar to ours, with both initial and final state identification, is by Ionikh *et al.*¹⁸ We will limit our comments to the work of these latter three groups.

As in Ref. 10, both the Setser and the Rosenwaks groups excited specific $N_2(B)$ levels in an afterglow and followed their time-resolved decay. The first group studied mainly the slower ($\geq 1 \mu s$) relaxation steps, while the second was able to resolve the fast collisional coupling between quaresonant levels. The results were in both studies interpreted mainly in terms of $N_2(B \leftrightarrow W)$ coupling, while little was said about the coupling with the A state. In Ref. 15 the involvement of $N_2(A)$ in the relaxation was doubted, although not ruled out. In Ref. 16, comparison with kinetic models indicated strong coupling of $N_2(B)$ mainly with $N_2(W)$, but in a few cases also with $N_2(A$ or $B')$.

Only in the work of Ionikh *et al.*¹⁸ was the $N_2(A \rightarrow B)$ transfer clearly identified as such. Similar to the present work, an entire vibrational level of the A state, $v''=7$, was depopulated by a laser pulse, and the subsequent reduction of the emission intensity from the coupled level B , $v'=0$ was observed. However, since this experiment was done using a decaying discharge afterglow, quantitative results were very difficult to obtain. The rate constant for the A , $7 \rightarrow B$, 0 energy transfer was derived from the decay kinetics of the B , 0 emission and thus depended on the time evolution of the A , 7 precursor level population. This is very critical, since the time scale of the observed process is comparable to that of the plasma decay (100–1000 μs). In fact, the rate constant of $0.5 \cdot 10^{-13} \text{ cm}^3/\text{s}$ derived for He is about 2 orders of magnitude lower than measured by us (for higher levels). This discrepancy is very likely due to unrecognized cascade processes feeding the (A , 7) level in the decaying plasma.

Comparisons of our results with those on the related systems CN and N_2^+ is also informative. The absolute cross sections measured for CN–Ar (Refs. 34, 35) and $N_2^+ - \text{He}$,^{36,37} and calculated for CN–He (Ref. 44) are generally found to be of the same order of magnitude, for close resonance, as measured by us. In the calculation^{43,44} a pronounced selectivity was found: For the A , $v=3 \rightarrow X$, $v=7$ process, having $\Delta E > 600 \text{ cm}^{-1}$, an extremely small ($\sim 10^{-5} \text{ \AA}^2$, though this may be inaccurate) cross section was found, compared to 0.1–1 \AA^2 for transitions with a ΔE ten times smaller. The recent experiments with Ar, however, indicated comparable cross sections for large and small ΔE .³⁵ These tendencies are very broadly in agreement with the present $N_2(A \rightarrow B)$ results, where the vibrational state selectivity decreases monotonically from He to Xe. The same trend is also observed for the $N_2(W \rightarrow B)$ transfer from Ar to Xe (the He and Ne data are here very inaccurate). Unfortunately, further comparisons are very limited since the experiments^{34–37} were made for only a few vibrational levels and only a single collision partner. In particular, the very striking increase of the extrapolated cross section σ_0 (for exact energy resonance) with the mass of the rare gas atoms cannot be compared to any other measurements or calculations.

Finally, we wish to emphasize that the near-resonant process is by no means the only conceivable mechanism of intramolecular energy transfer. A completely different, quasi-statistical product state distribution has, for example,

been observed in collisions of selectively laser excited Li_2 molecules with Li and rare gas atoms.⁵¹ Here long-lived complexes appear to be formed, whereas the present system represents a case of a “direct” type of interaction.

V. CONCLUSION

The present work reports on the first measurement of vibrational-state-to-state, absolute cross sections for collisional intramolecular electronic energy transfer from the $A^3\Sigma_u^+$ to the $B^3\Pi_g$ state of nitrogen. This process played for a long time an important role as one of the mechanisms postulated to explain the well-known Lewis–Rayleigh nitrogen afterglow.^{1–3} An unambiguous identification has, however, up till now never been given. In fact, in recent years the attention in the discussions of collisional coupling of $N_2(B)$ with other nitrogen triplet states shifted from the $A^3\Sigma_u^+$ to the $W^3\Delta_u$ state.^{8,11–13,15,16} In cell experiments and flow systems, the fast component of the time-resolved fluorescence decay from laser excited $N_2(B, v')$ levels was attributed to collisional coupling with another electronic (“dark”) state, and the W state was presumed to be the most likely candidate. The present work has shown that the A – B coupling is actually about equally important as the W – B coupling. Evidently, the time-resolved fluorescence technique under flow conditions is not sensitive enough to distinguish between the product states. Beam experiments such as the present one, on the other hand, guarantee the single-collision conditions necessary for a clear-cut identification of the reactant paths. In fact, this technique could in principle be extended to a comprehensive state specific study of all six possible pairwise collisional couplings between the four N_2 triplet states A , W , B , and B' . The B' state could be observed via its emission, while for the W state a suitable LIF detection scheme would still have to be developed.

In a broader context, the energy transfer process studied here is a relatively simple example of the general class of the “collision-induced internal conversion.” This mechanism has recently attracted much theoretical interest in studies of large, organic molecules,^{52,53} and has been abbreviated as CIIC, to distinguish it from the well-known spontaneous “internal conversion” (IC), which couples the vibrational manifold of different electronic states having the same spin multiplicity. Both IC and CIIC are extremely important pathways for the electronic/vibrational energy redistribution which controls the reaction dynamics of many large systems, for example, laser dyes. The present study of CIIC within the triplet system of a diatomic molecule can be viewed as an example of the extreme low level density situation, where individual initial and final vibrational states can be specified. It has been possible to explore in detail the effects of varying the energy gap and the collision partner, for two different electronic transitions, and to obtain absolute energy transfer cross sections for both of them under single collision conditions. It is hoped that this rather comprehensive study of a comparatively transparent coupling situation will prove useful in the further development of a better understanding of the CIIC phenomenon in general.

Note added in proof. The $N_2(G-W)$ transition addressed in the Introduction has now been observed by us in the spontaneous afterglow emission from the N_2^* beam [R. Bachmann, Ch. Ottinger, and A. F. Vilesov, J. Chem. Phys. (submitted)]. In Table III and Fig. 7, the He and Ne cross sections given for $v'=10$ should read 0.4 and 0.6 Å, respectively (instead of 0.6 and 0.9 Å). Very recent experiments have revealed an additional collisional pathway populating very selectively the $B, v'=10$ level from the $A', ^5\Sigma_g^+, v=0$ component of the N_2^* beam via a S/O perturbation of specific rotational/fine structure levels [Ch. Ottinger, L. G. Smirnova, and A. F. Vilesov, J. Chem. Phys. (in press)]. The contribution of this different CIAG mechanism to the total $B, v'=10$ population is about 30% for He and Ne, but is negligible for the heavier gases.

ACKNOWLEDGMENTS

This work was supported by the Deutsche Forschungsgemeinschaft, Sonderforschungsbereich 93. A. V. thanks the Alexander von Humboldt Foundation for a scholarship. The authors are indebted to Dr. Th. Glenewinkel-Meyer for the calculation of the Einstein coefficients.

APPENDIX A: DIRECT MEASUREMENTS OF THE DEPOPULATION

In an auxiliary experiment the degree of depopulation of the A -state levels in the N_2^* beam was measured directly by means of a pump and probe technique, employing two lasers. A narrow-band laser was used to probe the population of a particular A, v'' level with and without prior pumping by the broad-band laser pulse. The probe laser was fired with a delay of 30 μ s, to allow the LIF from the pump laser to decay. The lasers were here operated with Sulforhodamine 101 dye and were for convenience both tuned to similar wavelengths near 596 nm, in the $B, 8 \leftarrow A, 4$ band (while in all other experiments $\Delta v=5$ transitions were pumped). However, the probe laser could equally well have been tuned to a different transition out of the $v''=4$ level. LIF in the $B, 8 \rightarrow A, 5$ band was isolated by an appropriate interference filter. The two laser beams were superimposed by a wedge-shaped beam combiner and propagated parallel to each other and antiparallel with respect to the molecular beam. With the aid of the CCD camera inside the vacuum chamber the spatial coincidence of the two laser beams was adjusted in situ, and the diameters of the broad-band and narrow-band laser beams were measured to be 1 and 0.5 mm, respectively. Therefore, the narrow-band laser probes only a central part of the depopulated area of the molecular beam. Laser pulse energies were 1 mJ for the probing and 4 mJ for the depopulating laser, respectively. The collision cell was removed for these experiments. These measurements were made using a Stanford Research model SR 265 boxcar integrator (delay 0.5 μ s, gate 5 μ s).

Figure 11 shows the time-resolved LIF signals measured with and without depopulating the $A, v''=4$ level by the broad-band laser pulse. The probing laser was here set to a fixed wavelength at the P_{11} bandhead of the (8,4)

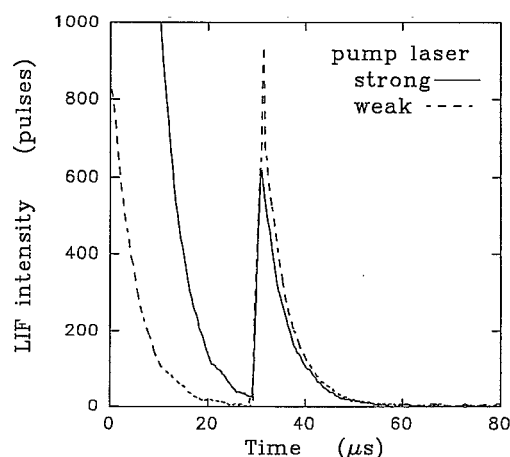


FIG. 11. Test of broad-band laser pumping efficiency. The LIF signals at $t=0$ and $t=30 \mu$ s are due to the pump and the probe laser, respectively, both operated at fixed frequency. A strong (4 mJ) preceding pump pulse reduces the probe signal by 22% in area.

transition, while the broad-band laser was adjusted to the center of the (8,4) band. (Actually, the broad-band laser was not entirely turned off for the run “without” laser pumping, but was greatly attenuated. This was more convenient because this laser beam provided a trigger signal for the delayed firing of the probe laser. The residual pump beam intensity is responsible for the LIF peak at $t=0$ in the dashed curve of Fig. 11. Comparing it with the very much larger peak at $t=0$ of the solid curve gives an impression of the extent of the pump beam attenuation.) The effect of the pumping can be seen on the probe laser LIF peak at 30–50 μ s. The solid curve, for the case of preceding depopulation of a “column” of molecules in the N_2^* beam, has an area 22% smaller than the dashed curve, measured essentially in the absence of optical pumping.

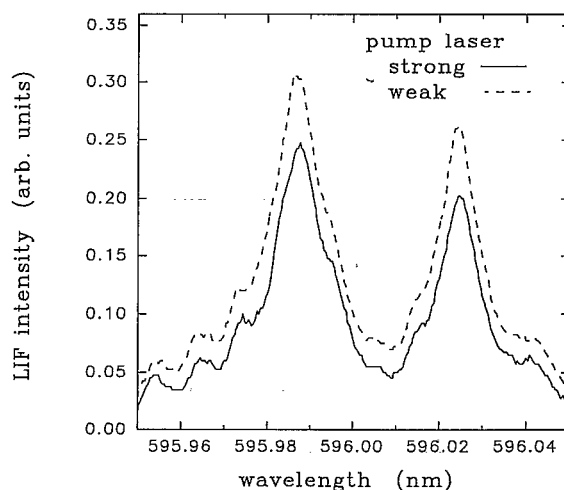


FIG. 12. Test of broad-band laser pumping efficiency as in Fig. 11, but scanning the 30 μ s delayed narrow-band probe laser across a 0.1 nm region of the (8,4) band. The average depletion of the lower ($v''=4$) level is consistent with that shown in Fig. 11.

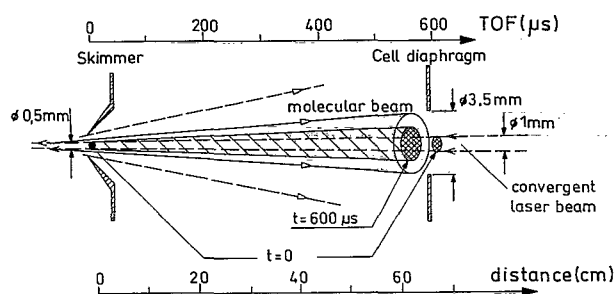


FIG. 13. Geometry of coaxial laser and molecular beam arrangement. At $t=0$ the laser depopulates a small fraction of the molecular beam inside the cell (small hatched area on the right), producing a small, instant CIAG dip. It also depopulates a relatively larger fraction of the beam in the region close to the skimmer (black dot on the left), which arrives at $t \sim 600 \mu\text{s}$ at the cell entrance diaphragm (large hatched area on the right) and produces the deepest portion of the CIAG dip (cf. Fig. 3).

While this experiment measures the magnitude of the optical pumping only at a fixed wavelength in the 8,4 band, Fig. 12 shows the LIF excitation spectrum, scanning the probe laser across a wavelength interval near the band-head, again with and without simultaneous pumping by the other laser. Here an average depopulation magnitude of 20% is read from the figure. The depletion is here somewhat smaller than the $\sim 30\%$ observed in Fig. 3 for the CIAG measurements with the same laser energy, because the Einstein coefficient for the (8,4) band is only about one-half of that in the $\Delta v=5$ sequence. Also, since the $B,8$ level is not predissociated, about 20% of the initially excited molecules decay radiatively back to $A,4$.

APPENDIX B: DEPOPULATION WAVE FORM AND AMPLITUDE

Figure 3 demonstrates a typical result of a depopulation experiment. Precisely at $t=0$ the CIAG should drop abruptly by a certain amount, due to the laser pumping of the $v''=16$ level. Unfortunately this drop was usually masked by a positive-going spurious signal resulting partly from the photomultiplier saturation by scattered laser light and partly from some short-lived phosphorescence which was apparently excited by scattered light on the surface of the collision cell and in the interference filter. This transient background signal depended strongly on the experimental conditions such as laser beam alignment and type of filter. It can be measured separately by turning the N_2^* beam off. This was actually done whenever CIAG data had to be taken at short times after the laser pulse (e.g., at $100 \mu\text{s}$, see below), and the background could then be subtracted out. In no case did it last longer than $\approx 200 \mu\text{s}$.

Accordingly, at $t \geq 100 \mu\text{s}$, the CIAG signal shown in Fig. 3 is clearly below the level I_0 and continues to decrease to a minimum, I_{\min} , at $t \approx 600 \mu\text{s}$. Thereafter it recovers to the constant level I_0 . This shape of the depopulation signal and its duration reflect the geometry of the experiment, see Fig. 13. Since the axes of the laser and the molecular beam coincide, $N_2(A)$ molecules are laser pumped along the entire length of the beam from the nozzle

to the collision cell. Therefore the depopulation signal lasts for approximately the time of flight of the molecules over this distance, which was in these experiments about $700 \mu\text{s}$. The tail end of the depopulation signal ($600 \leq t \leq 900 \mu\text{s}$) is not sharp due to the velocity distribution of the molecules in the beam.²³

On the other flank, for $0 \leq t \leq 500 \mu\text{s}$, the form of the CIAG signal is mainly determined not by the velocity distribution, but by geometry effects. The diameter of the molecular beam increases from 3.5 mm at $s=20 \text{ cm}$ to 14 mm at $s=70 \text{ cm}$. The diameter of the laser beam of $\approx 1 \text{ mm}$ is much smaller than the entrance diaphragm of the collision cell (3.5 mm). This was found to be important in order to avoid scattered light, which would, despite the interference filter, saturate the detector. Therefore, at $t=0$ only a small central part of the molecular beam is depopulated, and the drop of the CIAG signal at $t=0$ is relatively small. Close to the skimmer (at $s=0 \text{ cm}$, Fig. 13), the slightly focused laser beam pumps a $\approx 0.5 \text{ mm}$ diameter part of the molecular beam around its axis. However, when this section of the beam reaches the entrance diaphragm of the cell at $t=600 \mu\text{s}$, its diameter will be approximately four times larger due to the divergence of the molecular beam. It will then fill a large part of the entrance aperture of the collision cell. This magnification effect would produce a CIAG dip at $600 \mu\text{s}$ about 16 times larger than at $t=0$. The wave form shown in Fig. 3 is consistent with this estimate, within the large uncertainty of the extrapolation to $t=0$ made to eliminate the spurious signal during the first $100 \mu\text{s}$ (see above).

The general advantage of a collinear pumping geometry is the dramatic improvement of the duty factor of the experiment, since, essentially, a whole "column" of N_2^* is pumped. This is very important in view of the low CIAG intensity. In comparison with a perpendicular arrangement of the molecular and laser beam the gain amounts to a factor on the order of 10^3 .

Figure 3 demonstrates that a CIAG dip, relative to the continuous CIAG level, of 30% can be achieved. This is a lower limit to the actual relative depopulation of the $A, v''=16$ level by the laser. First, there may be other reactant levels contributing to the CIAG signal [$"Z_{v''}"$ in Eq. (3)], which are not affected by the laser. Second, not the entire cross section of the $N_2(A, v''=16)$ beam component entering the collision cell is laser pumped, not even at $t=600 \mu\text{s}$. Therefore, the observed CIAG dip represents a spatial average of the $v''=16$ depopulation, taken over the cross-sectional area of the beam including the unpumped fringe, and the depopulation on the beam axis will certainly be larger.

The dependence of this depletion on the laser pulse energy E is nonlinear due to the saturation of the transition, as would be expected considering the large observed depopulation. In the limit of strong laser fields, the relative depletion can be approximated as

$$\frac{\Delta[A, v'']}{[A, v'']} = \frac{1}{\alpha} \cdot \left\{ 1 - \exp \left[-\alpha \cdot \Delta T \cdot \int B_{v''}(\lambda) \cdot \rho(\lambda) \cdot d\lambda \right] \right\} \times (1 - A_{v''} \cdot \tau),$$

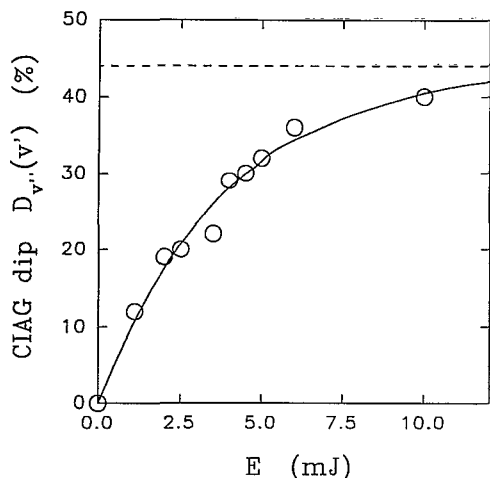


FIG. 14. Dependence of $D_{v''}(v')$, the dip of v' emission [Eq. (5) and (6)], on the power of the laser depopulating v'' . In the example shown, ($v''=16 \rightarrow v'=6$, argon) only this resonant process contributes to the CIAG, and $D_{16}(6)$ equals the relative depopulation $\Delta[4,16]/[4,16]$, times a geometry factor G . Since G , the depleted fraction of the beam cross sectional area, is < 1 (cf. Fig. 3), the asymptotic depletion is less than the theoretical maximum of 66.6%.

$$\alpha = (1 + g_A/g_B). \quad (\text{B1})$$

Here $B_{v''}(\lambda)$ is the absorption contour for the transition depopulating v'' at the laser wavelength λ . This function is normalized so that its integral over λ equals the Einstein coefficient. $A_{v''}$ is the Einstein coefficient for the reverse transition in spontaneous emission. $\rho(\lambda)$ is the spectral energy density of the laser pulse and ΔT is its length. The integration extends over the entire laser line profile. $g_A=3$ and $g_B=6$ are the statistical weights of the N_2 A and B states. τ is the lifetime, including predissociation, of the upper (B state) level of the laser-induced transition. The description of the saturation in the form of Eq. (B1) is of course oversimplified, since the absorption contour of the $B, v' \leftarrow A, v''$ transition is not homogeneous, but consists of numerous rotational lines.²¹ Strictly, the absorption of each individual rotational level should be considered, including the redistribution within the level manifold due to saturation effects, i.e., multiple, sequential absorption and stimulated emission events.

From Eq. (B1) it is seen that the theoretical maximum depopulation is determined only by the statistical weights of the A and B states, and is equal to 66.7%. Figure 14 shows the measured dependence of $D_{v''}(v')$ on the pulse energy E , for the same conditions as in Fig. 3 (observed level $B, v'=6$, pumped level $A, v''=16$, argon at $3 \cdot 10^{-3}$ mbar). A fit of Eq. (B1) to the experimental data gives an asymptotic high-energy limit of 44%. This is less than the calculated maximum mainly due to the geometry effect discussed above. Therefore, we have for the experimentally observable depletion

$$\Delta[A, v'']_{\text{eff}} = G \cdot \Delta[A, v''], \quad (\text{B2})$$

where, from the above data, $G=44/66.6=0.66$. Although the geometry factor G was determined for the particular

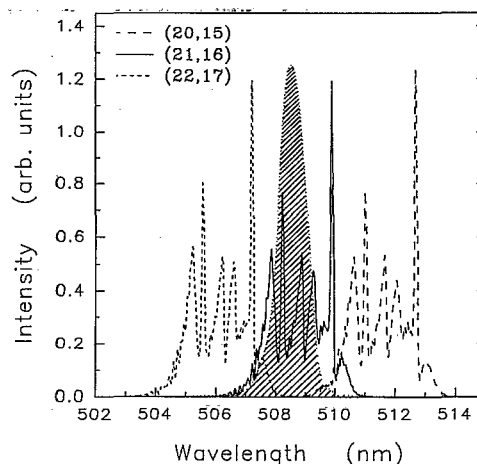


FIG. 15. Measured spectrum of the broad-band laser (hatched), overlapping the calculated absorption profile of the $\text{N}_2(B \leftarrow A)$ (21,16) band used to deplete $v''=16$. The two adjacent bands shown, with very small laser overlap, demonstrate the purity of the optical pumping.

case of $v'=6, v''=16$, it can be employed equally for all other levels. When the laser was tuned to a different v'' level, care was taken to ensure that the laser beam did not change its size or position. An additional confirmation of unaltered pump geometry was that the shape of the CIAG dip signal (cf. Fig. 3) did not change.

APPENDIX C: SELECTIVITY OF THE LASER PUMPING

The laser pumping may operate not only on the level v'' selected for depopulation, but to a small extent also on the adjacent levels. It is important to have quantitative data on this effect. A typical broad-band laser spectrum $\rho(\lambda)$ is shown in Fig. 15. It is centered on the $\text{N}_2(B \leftarrow A)$ (21,16) absorption band, the transition used to pump the $v''=16$ level in the experiments of Fig. 3 and Fig. 14. Calculated contours $B_{v''}(\lambda)$ of this and two other nearby bands, (22,17) and (20,15), are also given in Fig. 15. These band spectra were computer simulated for a Boltzmann rotational distribution with $T_{\text{rot}}(A)=140$ K. A fictitious “resolution” of 0.1 nm FWHM was assumed, which is sufficiently small compared to the laser bandwidth. In the computed spectra the line wavelengths in the 27 $\text{N}_2(B \leftarrow A)$ branches were calculated as described in Ref. 21. The line strengths were taken from the usual London–Hönl factors.³² Thus the different saturation of strong and weak lines was neglected, thereby allowing in a global way for the redistribution effects mentioned above.

For the example of Fig. 15, the extent of any interfering depopulation of the levels $v''=15$ and $v''=17$, relative to that of $v''=16$, was assessed using Eq. (B1) in the simplified form:

$$\frac{\Delta[A, v'']}{[A, v'']} = C_1 \cdot \left\{ 1 - \exp \left[-C_2 \cdot \int B_{v''}(\lambda) \cdot \rho(\lambda) \cdot d\lambda \right] \right\} = R_{v''}. \quad (\text{C1})$$

C_1 and C_2 are empirical coefficients obtained from the fit curve given in Fig. 5. It was then found from Eq. (C1) that the relative depopulation of the levels $v''=15,16,17$ was $R_{v''}=0.6\%, 28\%, 2.5\%$, respectively.

In the case of branching ratios which are very different from unity, the impurity excitation of the stronger branch will make a considerable contribution to the observed CIAG dip. The true branching ratio will then be greater than the raw data appear to indicate. An example is the population of $v'=7$ from $v''=17$ and 18 discussed below.

Numerically the impurity excitations are accounted for by replacing the term $\sigma_{A,v''}(v') \cdot R_{v''} \cdot [A, v'']$ in Eq. (6) [with Eq. (7)] by sums $\sum_{v''} \sigma_{A,v''}(v') \cdot R_{v''} \cdot [A, v'']$, extending over the range of v'' levels which are collisionally coupled with v' (e.g., $v''=17$ and 18 for $v'=7$). The calculated [Eq. (C1)] depopulations $R_{v''}$ now form a matrix, giving the depopulation of v'' when the laser is tuned to v'' . For example, in addition to the depopulations $R_{17,17} = 28.6\%$ and $R_{18,18} = 27.5\%$ given in Sec. III B, the off-diagonal elements $R_{17,18} = 2.1\%$ and $R_{18,17} = 0.7\%$ were calculated. The set of measured intensity dips $D_{v''}(v')$ for each laser setting v'' , e.g., $D_{17}(7)$ and $D_{18}(7)$, then yields an equal number of coupled linear equations for the cross sections $\sigma_{A,v''}(v')$. For example, dropping higher-order off-diagonal contributions, we find, instead of

$$\sigma_{17}(7) = C \cdot D_{17}(7) / (R_{17} \cdot [A, 17]), \quad (C2)$$

the corrected result

$$\sigma_{17}(7) = C \cdot \left[D_{17}(7) - \frac{R_{17,18}}{R_{18,18}} \cdot D_{18}(7) \right] / (R_{17,17} \cdot [A, 17]). \quad (C3)$$

In this example the cross section is reduced by 25% for $M=Kr$. This correction is one of the largest: The impurity depopulation of $v''=18$ with the laser set to $v''=17$, $R_{17,18}$, is fairly significant, and in addition it mixes the larger cross section, $\sigma_{18}(7)$, into the smaller one, $\sigma_{17}(7)$.

Similar calculations were performed for every v'' level which was laser pumped in this work. The respective laser spectra $\rho(\lambda)$ were monitored on-line on the CCD detector screen during the run. This was very important in order to maintain the optimum laser adjustment. A slight misalignment of the laser prism produces ASE emission which can appear far away from the laser peak wavelength. The laser was constantly manually realigned if it showed any signs of excessive ASE wings developing, which could have spread to the adjacent bands. The digitized laser spectrum was recorded for later use in the overlap calculations, Eq. (C1). Only those data were accepted where the impurity depletion of adjacent v'' levels did not exceed a few percent of that of the targeted v'' level. Note that the constants C_1 , C_2 in Eq. (C1), which were strictly only derived from the fit to the $v''=16$ depletion curve (Fig. 14), could safely also be used when applying Eq. (C1) to other groups of v'' levels.

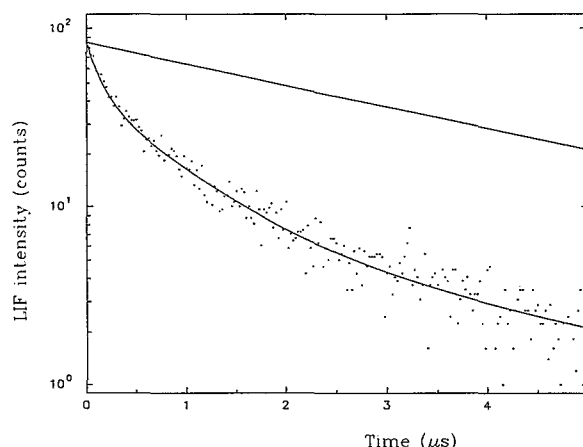


FIG. 16. Curve: (18,17) band LIF emission signal from the $A,13 \rightarrow B,18$ laser excitation (Fig. 6). An average background of two counts has been subtracted. The ordinate gives the average number of photon counts from five adjacent channels, each 5 ns wide. Data from 150 000 laser shots were accumulated, the total number of photon counts is 12 120. Straight line: Radiative decay in the absence of predissociation, $\tau_{\text{rad}}=3.6 \mu\text{s}$ (see the text).

APPENDIX D: DETAILS OF THE ABSOLUTE CROSS SECTION MEASUREMENTS

The procedure of the cross section measurements was the following: First, the usual CIAG dip measurement was performed, selecting the emission from $B, v'=4$ by a filter which transmits the (4,2) band. Then the photomultiplier was positioned so as to view a portion of the molecular plus laser beams *outside* the collision cell, 10 cm upstream. The filter was in this case substituted by one for the (18,17) band for the LIF emission, otherwise the detection geometry was identical. The displacement of the photomultiplier was essential to eliminate the scattered laser light which would otherwise, despite the (18,17) band filter, have completely obliterated the short-lived ($0 \leq t \leq 10 \mu\text{s}$) LIF signal (cf. the signals shown in Figs. 3–5 at short times). A 10 cm distance of the multiplier from the cell was found to be sufficient. On the other hand, this distance is short enough to ensure that the entire depopulated core of the beam as observed by LIF actually entered the cell without being attenuated by its entrance diaphragm (including, in particular, also the molecules excited by the fringe of the laser beam). Also, a larger distance would have introduced a spread of the arrival time of the laser-pumped molecules at the cell. Within the CIAG wave form (cf. Fig. 3) the CIAG intensity dip ΔI_v , which is relevant for the comparison with the LIF signal according to Eq. (9) is that at $t=100 \mu\text{s}$ after the laser pulse. This delay corresponds to the time of flight of the N_2^+ molecules between the two positions of the photomultiplier.

At $t=100 \mu\text{s}$ the CIAG dip is small, and moreover its direct measurement requires subtraction of the transient signal at $t=0$. Therefore, in most cases the dip was actually measured near $600 \mu\text{s}$, where it is most pronounced, and was scaled to its magnitude at $100 \mu\text{s}$. The two values are related to each other by a constant factor, since the shape

of the CIAG signal is independent of the collision gas or the v', v'' levels concerned. This factor was measured accurately using Xe, which gives the highest CIAG intensity, and was then applied to the other measurements.

In the measurement of I_{LIF} it is necessary to account quantitatively for the effect of predissociation of the upper state of the laser pumping transition. The predissociation of $\text{N}_2(B)$ was studied in Refs. 23 and 29, where it was found that its rate has a minimum at $B, v' = 17$ and 18. Thus these levels yield the highest LIF intensity. This is the reason for the particular choice of the levels in the calibration experiment. The result of the time-resolved LIF measurement for the first 5 μs is shown in Fig. 16. It is seen that the decay curve is multiexponential. This is the result of predissociation, under the present broad-band excitation conditions. In Refs. 23 and 29 it was shown that different S/O components of the $B, 18$ state have very different predissociation rates. The broad-band laser populates all these components at once. Therefore a composite decay of the overall $\text{N}_2(B, 18)$ fluorescence is observed. The curve is a three-component fit of the data points, with the assumed rate constants $\tau_1 = 3.6 \mu\text{s}$, $\tau_2 = 1.3 \mu\text{s}$, $\tau_3 = 0.136 \mu\text{s}$. Its only purpose is to establish the intercept at $t = 0$, therefore these τ values are not critical. The actual integrated LIF intensity was obtained as the sum of the recorded photon counts.

The straight line shows the purely radiative decay, such as would have been observed without predissociation. Its slope corresponds to a lifetime of $\tau_{\text{rad}} = 3.6 \mu\text{s}$. A value of $3.15 \mu\text{s}$ for this lifetime has been measured in time-resolved fluorescence experiments²⁹ using narrow-band pulsed excitation of the ${}^3\Pi_0^+$, $J' = 0$ level of $\text{N}_2(B, v' = 18)$ [via a $P_{13}(1)$ line]. This singular rotational- S/O level can be shown to be strictly unaffected by predissociation.²³ Unfortunately it was experimentally not possible to achieve a truly pure excitation of this particular level,²⁹ therefore the result is somewhat uncertain, and represents a lower limit of τ_{rad} . Nevertheless, it is in fairly good agreement with the lifetime as calculated from the Einstein coefficients for the $B, 18 \rightarrow A, v''$ transitions of interest. The latter were based on an *ab initio* calculation of the dependence of the transition moment on the internuclear distance,²⁵ normalized to experimentally measured $\text{N}_2(B, v')$ radiative lifetimes.³⁰ The *ab initio* calculations are, in turn, supported by a recent, but less comprehensive experimental determination of the transition moment function.²⁶ The calculations gave a lifetime of $\tau_{\text{rad}} = 4.0 \mu\text{s}$ for the $v' = 18$ level. In our analysis we use the mean, $3.6 \mu\text{s}$, of the experimental and the theoretical result.

The intensity of the calculated radiative decay curve in Fig. 16 is normalized so as to coincide with the experimental curve at $t = 0$, because immediately after excitation by the laser pulse the LIF intensity emitted by the ensemble of excited molecules is the same, whether predissociation is present or not. (Remember at this point that the predissociation of the $v' = 18$ level is exceptionally slow, with an inverse rate much larger than the laser pulse width). Then the area under this straight line is proportional to the integral LIF intensity in the absence of predissociation, i.e.,

to the actual depopulation of the A, v'' level. From Fig. 16 it was found that the measured integral LIF intensity has to be multiplied by a factor of $f = 5.0 \pm 0.5$ in order to correct for the light loss due to predissociation of the $B, v' = 18$ level.

Note that the correction factor f , and therefore from Eq. (9) [or specifically Eq. (D1)] also the ultimate cross section result, depends linearly on the value of τ_{rad} , because of $\int_0^\infty \exp(-t/\tau) dt = \tau$. It is therefore important that, in addition to several, consistent determinations of the transition moment function, the direct measurement of τ_{rad} from Ref. 29 is also available, at least for $v' = 18$. From a comparison of the theoretical and the experimental value of τ_{rad} , the uncertainty of the absolute cross sections from this source is estimated as $\pm 10\%$.

Expression (9) for the case at hand, i.e., the cross section for the collision-induced transition from $A, 13$ to $B, 4$, now reads in full

$$\sigma_{A,13}(4) = \frac{\Delta I_4(4,2)/\Delta t}{I_{\text{LIF}}(18,17) \cdot f} \cdot \frac{\sum_{v''} A_{4,v''}/A_{4,2}}{\sum_{v''} A_{18,v''}/A_{18,17}} \cdot \frac{\int F_{653}(\lambda) \cdot S_{18,17}(\lambda) d\lambda}{\int F_{750}(\lambda) \cdot S_{4,2}(\lambda) d\lambda} \frac{\eta(653)}{\eta(750)} \cdot \frac{1}{[M] \cdot \bar{v}_{\text{rel}}} \quad (\text{D1})$$

Compared to Eq. (9), both the decrease ΔI_4 of the CIAG emission from $v' = 4$ and the LIF intensity are here labeled explicitly by the respective bands on which they were detected. Specifically, $\Delta I_4(4,2)$ was obtained as the number of CIAG photon counts in the multichannel memory, summed over some short time interval from $100 \mu\text{s} - \Delta t/2$ to $100 \mu\text{s} + \Delta t/2$ after the laser pulse, minus the number of photon counts summed over an equal interval, but for the steady-state CIAG intensity as observed a long time (2 ms) after the laser pulse. The difference signal, being proportional to the arbitrary time interval Δt (e.g., $\Delta t = 50 \mu\text{s}$), is normalized to Δt in Eq. (D1). $I_{\text{LIF}}(18,17)$, the integrated LIF signal, is simply the total number of LIF photon counts from $t = 0$ to $10 \mu\text{s}$, where the LIF signal disappears in the noise level. Both $\Delta I_4(4,2)$ and I_{LIF} were normalized to the same number of laser shots (typically 50 000). $f = 5.0$ is the predissociation correction discussed above. Thus the first term of Eq. (D1), of dimension s^{-1} , is the raw result for the rate of the collision-induced energy transfer. The second to fourth terms are spectroscopic corrections. The second term allows for the fact that of the total CIAG and the LIF emission only one band in each case is actually observed. The $A_{v',v''}$ are the corresponding Einstein coefficients. The third term accounts for the transmission functions $F(\lambda)$ of the filters used for the CIAG and LIF detection, centered at 750 and 653 nm, respectively. In the overlap integrals with the respective emission band contours, $S_{4,2}(\lambda)$ and $S_{18,17}(\lambda)$, $F(\lambda)$ is in percent, and $\int S(\lambda) d\lambda$ is normalized to unity. The fourth term is the ratio of the photomultiplier quantum efficiencies at the center of the filter band widths, taken from the PM spec-

TABLE V. Vibrational molecular constants (in cm^{-1}) of the $B^3\Pi_g$ and $A^3\Sigma_u^+$ states of N_2 .

	$B^3\Pi_g$	$A^3\Sigma_u^+$
T_e	9415.0714	
ω_e	1734.034	1460.589
$\omega_e x_e$	14.416	13.840
$\omega_e y_e$	$-2.563 \cdot 10^{-3}$	$5.229 \cdot 10^{-3}$
$\omega_e z_e$	$-8.475 \cdot 10^{-4}$	$-1.9475 \cdot 10^{-3}$
$\omega_e u_e$	$4.331 \cdot 10^{-5}$	$4.6148 \cdot 10^{-5}$
$\omega_e v_e$	$-1.689 \cdot 10^{-6}$	$-2.5017 \cdot 10^{-6}$

ifications. The last term converts the rate of the collision-induced process to a cross section, cf. Eq. (4).

APPENDIX E: CROSS SECTION PARTITIONING

Consider the case that in addition to a nearest-to-resonance level A_0 two other levels A_1, A_2 contribute, the respective cross sections being $\sigma_0, \sigma_1, \sigma_2$. Then we have for the undifferentiated cross section σ_{rel} from Ref. 19, ascribed in that work entirely to the A_0 channel

$$\sigma_{\text{rel}} \cdot [A_0] = \sum_{i=0}^2 \sigma_i \cdot [A_i]. \quad (\text{E1})$$

With the branching ratios $f_1 = \sigma_1/\sigma_0$ and $f_2 = \sigma_2/\sigma_0$ measured in the present experiments and the relative level populations $[A_i]$ from Eq. (8) we then find

$$\sigma_0 = \frac{\sigma_{\text{rel}}}{1 + f_1 \cdot [A_1]/[A_0] + f_2 \cdot [A_2]/[A_0]},$$

$$\sigma_1 = f_1 \cdot \sigma_0, \quad \sigma_2 = f_2 \cdot \sigma_0. \quad (\text{E2})$$

These partial cross sections are then made absolute via Eq. (10).

A special situation occurs for $v' = 7$. In the earlier work equal contributions from the roughly equidistant levels $v'' = 17$ (435 cm^{-1} endothermic) and $v'' = 18$ (483 cm^{-1} exothermic) were assumed, and the measured relative cross section was normalized to the sum of the populations $[A, 17] + [A, 18]$. The present branching ratio measurements show, however, that the endothermic channel contributes very little, and the cross sections for $A, 18 \rightarrow B, 7$ are, instead, about twice as large as is obtained through Eq. (14) from the σ_{rel} given in Ref. 19, Fig. 11.

APPENDIX F: MOLECULAR CONSTANTS FOR THE A AND B STATES

In order to interpret the measured cross sections in terms of the nitrogen molecule energies involved, the latter must be reliably known up to high vibrational levels of the A state. The same is true also for the B state in order to ensure the correct tuning of the depopulating laser to the desired transition. Very accurate spectroscopic data have been published up to $v'' = 8$ in the A state and $v' = 12$ in the B state.⁵⁴ For the best possible description of the high levels studied in this work, we have used vibrational mo-

lecular constants from Ref. 33 which were obtained as a weighted least-square fit of the combined spectroscopic data from Refs. 23, 33, 54, and 55. They include levels as high as $A, 21$ and $B, 26$. These data are presented in Table V, and are the basis for Fig. 1.

- ¹M. Campbell and B. A. Thrush, Proc. R. Soc. London, Ser. A **296**, 201 (1967).
- ²M. F. Golde and B. A. Thrush, Faraday Discuss. Chem. Soc. **53**, 58 (1972).
- ³E. M. Gartner and B. A. Thrush, Proc. R. Soc. London, Ser. A **346**, 103, 121 (1975).
- ⁴D. S. Bistrov, A. F. Vilesov, A. M. Pravilov, and L. G. Smirnova, Sov. J. Chem. Phys. **6**, 2306 (1990) [Khim. Fiz. **6**, 1173 (1987)]; A. F. Vilesov, A. M. Pravilov, and L. G. Smirnova, *ibid.* **6**, 2326 (1990); **6**, 2797 (1990) [Khim. Fiz. **6**, 1183 (1987); **6**, 1421 (1987)].
- ⁵M. Jeunehomme, J. Chem. Phys. **45**, 1805 (1966).
- ⁶T. A. Carson, N. Duric, P. Erman, and M. Larson, Phys. Scr. **19**, 25 (1979).
- ⁷Yu. Z. Ionikh and N. V. Chernysheva, Opt. Spectrosc. (USSR) **68**, 598 (1990).
- ⁸W. Benesch, J. Chem. Phys. **78**, 2878 (1983); J. S. Morrill, W. M. Benesch, and K. G. Widing, *ibid.* **94**, 262 (1991).
- ⁹L. G. Piper, J. Chem. Phys. **97**, 270 (1992).
- ¹⁰R. F. Heidner III, D. G. Sutton, and S. H. Suchard, Chem. Phys. Lett. **37**, 243 (1976).
- ¹¹N. Sadeghi and D. W. Setser, Chem. Phys. Lett. **77**, 304 (1981).
- ¹²A. Rotem, I. Nadler, and S. Rosenwaks, Chem. Phys. Lett. **83**, 281 (1981).
- ¹³D. Cerny, R. Bacis, R. W. Field, and R. A. McFarlane, J. Phys. Chem. **85**, 2626 (1981).
- ¹⁴A. Rotem, I. Nadler, and S. Rosenwaks, J. Chem. Phys. **76**, 2109 (1982).
- ¹⁵N. Sadeghi and D. W. Setser, J. Chem. Phys. **79**, 2710 (1983).
- ¹⁶A. Rotem and S. Rosenwaks, Opt. Eng. **22**, 564 (1983).
- ¹⁷A. Ali and P. J. Dagdigian, J. Chem. Phys. **87**, 6915 (1987).
- ¹⁸Yu. Z. Ionikh, N. P. Penkin, N. V. Chernysheva, and O. G. Yartseva, Opt. Spectrosc. (USSR) **65**, 25 (1988).
- ¹⁹R. Bachmann, X. Li, Ch. Ottinger, and A. F. Vilesov, J. Chem. Phys. **96**, 5151 (1992).
- ²⁰D. Neuschäfer, Ch. Ottinger, and A. Sharma, Chem. Phys. **117**, 133 (1987).
- ²¹H. Geisen, D. Neuschäfer, and Ch. Ottinger, Z. Phys. D **4**, 263 (1987).
- ²²H. Geisen, D. Neuschäfer, and Ch. Ottinger, Z. Phys. D **17**, 137 (1990).
- ²³H. Geisen, D. Neuschäfer, and Ch. Ottinger, J. Chem. Phys. **92**, 104 (1990).
- ²⁴D. E. Shemansky and N. P. Carleton, J. Chem. Phys. **51**, 682 (1969); D. E. Shemansky, *ibid.* **51**, 689 (1969).
- ²⁵H.-J. Werner, J. Kalcher, and E. A. Reinsch, J. Chem. Phys. **81**, 2420 (1984).
- ²⁶L. G. Piper, K. W. Holtzclaw, and B. D. Green, J. Chem. Phys. **90**, 5337 (1989).
- ²⁷Varian Ion gauge 890-AR C.U. Instruction manual.
- ²⁸Ch. Ottinger, A. Slenczka, and V. Wulfmeyer, Appl. Opt. (submitted).
- ²⁹R. Ehlich, Diploma thesis, MPI für Strömungsforschung, Göttingen, 1990.
- ³⁰E. E. Eyler and F. M. Pipkin, J. Chem. Phys. **79**, 3654 (1983).
- ³¹R. Bachmann, Ch. Ottinger, and A. F. Vilesov, Chem. Phys. Lett. **203**, 314 (1993).
- ³²T. Kovacs, *Rotational Structure and the Spectra of Diatomic Molecules* (Adam Hilger, London, 1968).
- ³³H. Geisen, Dissertation, MPI für Strömungsforschung, Göttingen, 1989.
- ³⁴D. H. Katayama, T. A. Miller, and V. E. Bondybey, J. Chem. Phys. **71**, 1662 (1979).
- ³⁵G. Jihua, A. Ali and P. J. Dagdigian, J. Chem. Phys. **85**, 7098 (1986).
- ³⁶D. H. Katayama, A. V. Dentamaro, and J. A. Welsh, J. Chem. Phys. **87**, 6983 (1987).

- ³⁷D. H. Katayama and A. V. Dentamaro, *J. Chem. Phys.* **91**, 4571 (1989).
- ³⁸D. H. Katayama and J. A. Welsh, *Chem. Phys. Lett.* **106**, 74 (1984).
- ³⁹V. E. Bondybey and T. A. Miller, *J. Chem. Phys.* **69**, 3597 (1978).
- ⁴⁰D. H. Katayama and J. A. Welsh, *J. Chem. Phys.* **79**, 3627 (1983).
- ⁴¹A. V. Dentamaro and D. H. Katayama, *J. Chem. Phys.* **90**, 91 (1988).
- ⁴²A. M. Pravilov, L. G. Smirnova, and A. F. Vilesov, *Chem. Phys. Lett.* **144**, 469 (1988).
- ⁴³H.-J. Werner, B. Follmeg, and M. H. Alexander, *J. Chem. Phys.* **89**, 3139 (1988).
- ⁴⁴H.-J. Werner, B. Follmeg, M. H. Alexander, and D. Lemoine, *J. Chem. Phys.* **91**, 5425 (1989).
- ⁴⁵A. Loftus and P. H. Krupenie, *J. Phys. Chem. Ref. Data* **6**, 113 (1977).
- ⁴⁶V. Aquilanti, R. Candori, F. Pirani, T. Krümpelmann, and Ch. Ottinger, *Chem. Phys.* **142**, 47 (1990). Here the analogy of N_2^* with NO is discussed. For NO interaction potentials see the following two references.
- ⁴⁷H. H. W. Thuis, S. Stolte, J. Reuss, J. J. H. van den Biesen, and C. J. N. van den Meijdenberg, *Chem. Phys.* **52**, 211 (1980).
- ⁴⁸A. A. Radzig and B. M. Smirnov, *Reference Data on Atoms, Molecules and Ions*, Springer Series in Chemical Physics 31 (Springer, Berlin, 1988), p. 410.
- ⁴⁹E. Bauer, E. R. Fisher, and F. R. Gilmore, *J. Chem. Phys.* **51**, 4173 (1969).
- ⁵⁰W. L. Jorgensen and L. Salem, *The Organic Chemist's Book of Orbitals* (Academic, New York, 1974).
- ⁵¹G. Ennen and Ch. Ottinger, *J. Chem. Phys.* **76**, 5812 (1982).
- ⁵²K. F. Freed, *Adv. Chem. Phys.* **47**, 291 (1981).
- ⁵³A. Tramer and A. Nitzan, *Adv. Chem. Phys.* **47**, 337 (1981).
- ⁵⁴F. Roux, F. Michaud, and J. Verges, *J. Mol. Spectrosc.* **97**, 253 (1983).
- ⁵⁵A. Y.-M. Ung, *J. Chem. Phys.* **65**, 2987 (1976).